CORA Cork Open Research Archive
Cartlann Taighde Oscailte Chorcaí

Title	Investigation of a wearable compliant mechanism for knee rehabilitation
Authors	Chen, Yingyue
Publication date	2021-04-20
Original Citation	Chen, Y. 2021. Investigation of a wearable compliant mechanism for knee rehabilitation. MRes Thesis, University College Cork.
Type of publication	Masters thesis (Research)
Rights	© 2021, Yingyue Chen. - https://creativecommons.org/licenses/by-nc-nd/4.0/
Download date	2026-11-03 13:54:54
Item downloaded from	https://hdl.handle.net/10468/11912

UCC
University College Cork, Ireland
Coláiste na hOllscoile Corcaigh

Ollscoil na hÉireann, Corcaigh

National University of Ireland, Cork



Investigation of a wearable compliant mechanism for knee rehabilitation

Thesis presented by

Yingyue Chen

for the degree of

MEngSc (Research) - Mechanical Engineering

University College Cork

School of Engineering and Architecture - Electrical and Electronic Engineering

Head of School/Department: Prof. Jorge Oliveira

Supervisor(s): Dr. Guangbo Hao, Dr. Zili Li

April 2021

Abstract

Wearable devices for knee rehabilitation have been studied extensively in the past few years, with particular applications in tackling ageing problems all over the world. Such devices were firstly created 40 years ago. Although numerous solutions have been proposed since then, many challenges still exist, like high energy consumption compared to their short battery lifetime, low portability and incompatibility anthropomorphic mechanisms.

Recently, these issues are resolved with different methods, including the development of better-designed actuators and artificial muscles, and the improvement of gait models. However, there are questions associated with each of these methods such as the self-weight of actuators and muscles which decrease the portability of the devices, while increased complexity is associated with more accurate models.

The resulting device from this thesis aims to overcome the difficulties mentioned above and acts as lightweight and functional wearable devices/joints. The device consists of two rings fixed on the femur and tibia, respectively, connected with two crossing flexural shells. The design concept comes from the anatomy and physiology of the human knees concluded in the bio-joint model. Two designs, cross-spring pivot and the crossing four-bar linkage, are studied in this thesis. The kinetostatic models of the two designs are established for the intended bionic characteristics. After optimizing the two designs by using the analytical models, it shows that the crossing four-bar linkage is much better than the cross-spring pivot for matching the bio-joint. A comparison between analytical model and FEA for each design is implemented, showing acceptable agreement. A prototype is fabricated, and preliminarily static experiment tests are conducted.

Acknowledgements

I would like to acknowledge and extend my gratitude to the following persons who have made the completion of this project possible:

- Dr. Guangbo Hao for his help and supervision throughout the entire project and for always making himself available for meetings and discussions.
- Dr. Zili Li for his civil engineering expertise, continuous input into the structures and material of the mechanism and for being available for monthly discussions and meeting.
- Dr. Jiajie Guo for his help and guidance in knee kinematic analysis, in particular for the codes he gave in assisting to overcome the programming associated with Matlab.
- Mr. Timothy Power and Mr. Michael O'Shea for their technical support, displaying incredible skills and patience in fabricating various prototypes.
- I would like to thank my many colleagues in particular Ms. Shiyao Li, Mr. Haitong Liang, and Mr. Jiaxiang Zhu who assisted in formula derivation, model simulation and testing material support.
- Finally I would like to thank my friends and family who supported me throughout this project.

Declaration of Authenticity

The work described in this thesis was conducted by the author, except when stated otherwise, in the School of Electrical and Electronic Engineering between January 2020 and April 2021. This thesis was written entirely by the author, except where stated otherwise. The source of any material not created by the author has been clearly referenced.

Signed: Yingyue Chen Date: 20/4/2021

Table of Contents

Abstract I

Acknowledgements II

Declaration of Authenticity III

Table of Contents IV

List of Figures VI

List of Tables IX

1. Introduction 1

1.1. Overview of the lower limb exoskeletons for knee rehabilitation 1

1.2. Challenge and inspiration 4

1.3. Project proposal 6

2. Knee joint analysis 8

2.1. Complex function of the knee joint 8

2.2. Sliding-rolling ratio 10

2.3. Bio-joint analysis 11

3. Modeling of two compliant mechanisms 14

3.1. The generalized cross-spring pivot 14

3.1.1. The centre shift of the generalized cross-spring pivot 15

3.1.2. Accuracy analysis of the generalized cross-spring pivot 17

3.2. The crossed four-bar linkage 18

3.2.1. Four-bar linkage 18

3.2.2. Kinematics of rigid four-bar linkage 18

3.2.3. The flexural hinges replacement of the crossing four-bar linkage 21

4. Mechanisms optimization 25

4.1. Cross-spring pivot 25

4.1.1. The optimization methods 25
4.1.2. FEA simulation 26
4.1.3. Comparison 29
4.2. Crossing four-bar linkage 32
4.2.1. The optimization methods 33
4.2.2. FEA simulation 34
4.2.3. Comparison 36
5. Prototype design and testing 40
5.1. Mechanism design 40
5.1.1. Mechanism design based on cross-spring pivot 40
5.1.2. Mechanism design based on crossing four-bar linkage 41
5.2. Fabrication and testing 42
5.2.1. Fabrication 42
5.2.2. Demonstration 44
5.2.3. Testing 44
5.3. Discussions 48
6. Future work and conclusions 50
6.1. Future work 50
6.2. Conclusions 50
7. References 52
8. Appendices 55
8.1. Matlab code for optimizing cross-spring pivot 55
8.2. Matlab code for optimizing four-bar linkage 57

List of Figures

Figure 1 Lower Limb Exoskeletons and Exosuits.[5] 1

Figure 2 The structure of the cruciate ligament of the knee joint.[16][17] 5

Figure 3 Snapshots of the bio-joint.[19] 7

Figure 4 Four-bar linkage system: **a** Illustration of the Burmester curve and four-bar linkage system, and **b** Illustration of ACL and PCL with medial and lateral menisci.[21] 8

Figure 5 Knee joint has six degree of freedom for rotation and translation.[21] 9

Figure 6 Movement of the femur relative to the tibia during flexion: **a** Pure rolling, **b** Pure gliding, **c** Combination of rolling and gliding.[22] 10

Figure 7 Plots of normalized rolling and sliding displacements. 10

Figure 8 Snapshots of an exoskeleton of bio-joint model. 11

Figure 9 Comparison of displacements of centre point and end point. 12

Figure 10 The rotational centre point of bio-joint: **a** The trajectory of bio-joint rotational centre, and **b** The displacement of bio-joint rotational centre. 13

Figure 11 The relationships between loads and displacements for a generalized cross-spring pivot: **(a)** A deflected generalized cross-spring pivot, and **(b)** The exploded view for the loads and displacements.[33] 17

Figure 12 A coupler-driven four-bar linkage.[37] 19

Figure 13 The model of the asymmetric crossing four-bar linkage.[34] 20

Figure 14 The fixed-guided flexible segment: **a** Flexible beam, and **b** Pseudo-Rigid-Body Model.[38] 21

Figure 15 The model of the asymmetric crossing four-bar linkage (with moment).[34] 22

Figure 16 The logic flowchart of the optimization (cross-spring pivot). 26

Figure 17 FEA simulation (cross-spring pivot): **a** Front view of the model, **b** Hex Dominant Meshing, **c** Simulation demonstration. 28

Figure 18 The geometric relationship between endpoints $A1, A2$ and rotational centre O'.[39] 29

Figure 19 The comparison between bio-joint and cross-spring pivot (theoretical results without p). 30

Figure 20 The comparison between bio-joint and cross-spring pivot (FEA results without p). 30

Figure 21 The comparison between bio-joint and cross-spring pivot (theoretical results with p). 31

Figure 22 The comparison between bio-joint and cross-spring pivot (FEA results with p). 32

Figure 23 The logic flowchart of the optimization (crossing four-bar linkage). 33

Figure 24 FEA simulation (flexural four-bar linkage): **a** Front view of the model, **b** Hex Dominant Meshing, **c** Simulation demonstration 35

Figure 25 The comparison between bio-joint and four-bar linkage (theoretical results of the rigid joints). 37

Figure 26 The comparison between bio-joint and four-bar linkage (FEA results of flexural joints). 37

Figure 27 The comparison between FEA results and virtual work calculation (the moment-rotation relationship) 38

Figure 28 The assembly drawing of the cross-spring pivot model: **a** Front view, and **b** Isometric view. 40

Figure 29 Adjustable laces inspiration. 41

Figure 30 The assembly drawing of the crossing four-bar model: **a** Front view, and **b** Isometric view. 41

Figure 31 The details of the connection. 42

Figure 32 Prototype: **a**, **b** the local details of the device, and **c** the assembled mechanism. 43

Figure 33 The demonstration. 44

Figure 34 Experimental materials. 45

Figure 35 Experimental process: **a**, **b**, **c** Adding 10g, 20g, and 30g weights on the platform, respectively. 45

Figure 36 Experimental results. 46

Figure 37 Comparison between FEA and experimental results: **a** the FEA simulation, and **b** the comparison between theoretical, FEA results and the bio-joint. 47

Figure 38 Inversion-based four-bar linkage. 48

List of Tables

Table 1 Comparison of passive devices. 2

Table 2 Physical parameters of human's lower leg. 12

Table 3 The material parameters of beryllium bronze. 27

Table 4 The value of optimized parameters (cross-spring pivot). 29

Table 5 The values of optimized parameters (four-bar linkage). 36

Table 6 The printer technical specifications. 42

Table 7 The experimental results. 45

1. Introduction

1.1. Overview of the lower limb exoskeletons for knee rehabilitation

Rehabilitation medical experiment has proved that concentration and repeatability of task-oriented rehabilitation exercise training can rebuild the related functions of the nervous system, and can enhance muscle strength, enabling the patient to move independently again. Many patients worldwide suffer the pain of the knee impairments such as muscle weakness, paralysis and gait disorders, which might be caused by a stroke, spinal cord injury or post-polio.[1] The long period of physical therapies cost huge sums of time and money as well as regular commuting between hospitals and home. Therefore, there is a great need for wearable rehabilitation robots.[2]

Lower limb exoskeletons (LLEs) have been studied extensively for a wide range of applications in rehabilitation for assisting human walking (Fig. 1). As the important transmission segment between the hip joint and the ankle joint, the knee joint needs to support the body's huge portions of weight. In order to efficiently reduce the knee payload, which is recognized as an important factor for knee pain and disorder, passive knee exoskeletons (KEs) have been designed to suit patients who suffer from knee pain but still can walk slowly.[3] In contrast to active KEs, a passive KE has simpler structures, lower production costs, and requires no electric power at all, thus making it more practical and promotable than active KEs.[4]



Figure 1 Lower Limb Exoskeletons and Exosuits.[5]

According to the use of different structures, the passive KEs can be divided into categories as follows. The 4-bar linkage is one of the typical structures implemented to resemble the polycentric motion of human knees as reported by Chaichaowarat et al.[6], and its structures are always simple. Spring mechanisms are utilized to store and release energy to reduce the quadricep effort presented in passive KEs. Due to the fact that a torsion spring always generates the moment as a proportion of the angular displacement, the basic mechanical component can simultaneously act as an angular position sensor and a joint actuator, which is handy for a compact design of the exoskeleton.[7] In addition to the above structures, a compliant-mechanism-based design, developed by Ranaweera et al.[8] is another representative passive KE. They assume the body shape over the frontal plane if contact forces are significantly high, thus, reducing the possibility of internal joint injuries due to misalignments.[8] Despite much progress in the field of assistive robotic technologies, such as power sources, small and sensitive sensors, there is still a need to develop a lightweight, simple-structure, self-adaptive exoskeleton.

Table 1 provides an overview of the passive KEs over the last decade. Several structures are tabulated, each elaborated in terms of the working principle and features.

Table 1 Comparison of passive devices.

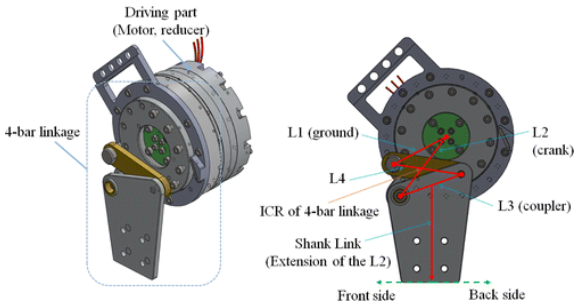
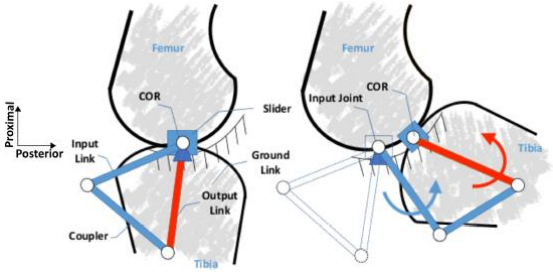
Structure	Appearance	Working principle	Feature
4-bar linkage	 a[9]	As the crank rotated, the instant center of rotation (COR) changes as the path similar to knee motion.	Accommodate comfort and keep binding force according to reduce friction.
2 degree of freedom (DoF) 5-bar linkage	 b[10]	The coupler motion of rotation and translation was achieved by a slider which transferred the torque from the input to the output.	Avoid mismatch between limb joint mand mechanical interface motion.

Table 1 (continued).

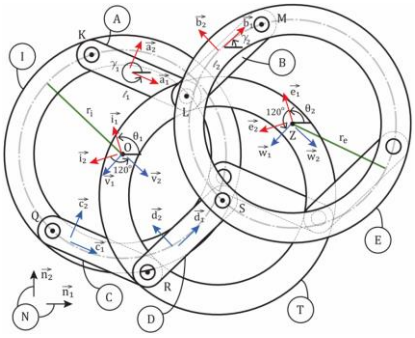
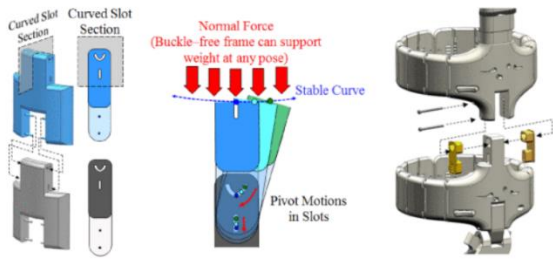
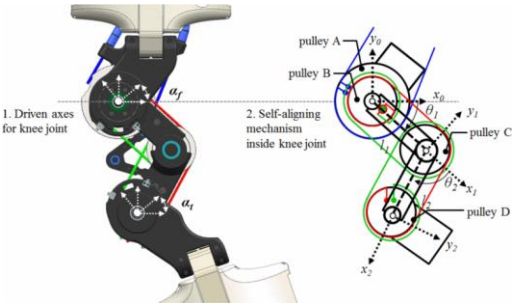
Schmidt coupling	 c[11]	The mechanism contained 1 active rotational DoF given by Bowden cable and 2 passive translational DoF which offered the knee flexion and extension and measured the anterior-posterior (AP) translation.	Enables active rotations, and passive translations of the COR Higher rigidity and position accuracy.
Soft exosuit	 d[12]	The soft exosuit consisted of 2 inflatable soft actuators with an I cross-section, which made an equal lever arm around the knee joint when inflated, providing great support for knee motion. Hook and loop straps adjusting comfort and fit also distributed the force to the femur and tibia.	Enhance the compliance between human and device.
Buckle-free frame	 e[13]	Composed of 2 links with slots and connection pins. 1 curved slot and 1 vertical slot and 2 connection pins achieved the specified motion (concave motion).	Flexible and load-sustainable.

Table 1 (continued).

Pulleys and links	 f[14]	Composed of a driving pulley, 3 aligning pulleys, 2 aligning links, with a thigh link and a shank link, respectively. Therefore, it has 1 active and 2 passive DoF. Two parallelograms created by 2 links, 3 pulleys and a cable transferred orientation and torque from thigh to shank, and controlled by angle sensors.	Individual deviation is independent of body.
Compliant rings	 g[15]	The outer and inner compliant rings connected to the upper and lower links respectively. The shape of the rings would be deformed cater to knee motion during swing, but would be rigid during stance and the slider-spring would also support the body weight.	Accommodates kinematic differences between human knee and mechanical joint, and supports human bodyweight during walking.

1.2. Challenge and inspiration

These mechanisms are shown in Fig. 2 still have the problems associated with heavy-shape, low-portability, and non-adaptability to the human joint.

1. Non-adaptable solution

With the unsuitable exoskeletons which are used to improving strength and endurance, it will cause discomfort and pain on the knee, which may even hurt the internal tissue and limit the

range of motion, giving rise to joint dysfunctionality. Thus, investigation of the kinematics and biomechanics on the knee is vital significant before designing the model.

The current research has demonstrated that the motion of the knee is motived by the cruciate ligament established through the asymmetric crossing four-bar linkage shown in Fig. 2. This mechanism with the different lengths and original angles of four bars can be derived from the generalized four-bar linkage, but with some differences. The instantaneous centre of rotation (ICR) of this mechanism changes its position with the angle of flexion, also known as centre shift, which is similar to the human knee's motion. Therefore, we can simulate the structure of asymmetric crossing four-bar linkage while we design the model.

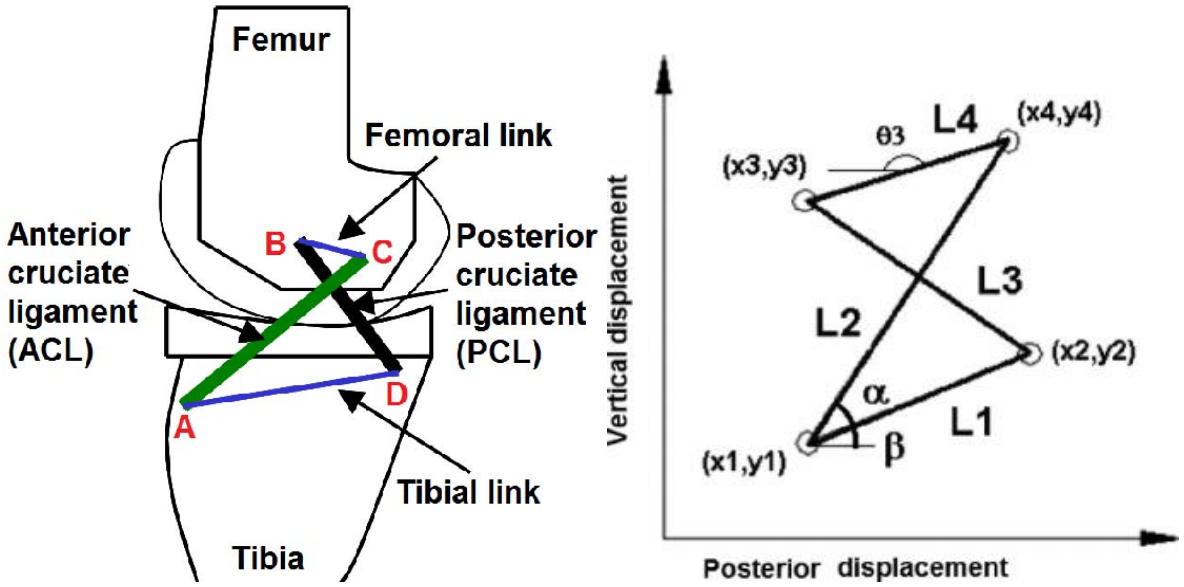


Figure 2 The structure of the cruciate ligament of the knee joint.[16][17]

2. Heavy-shape and complex-assembly solution

A conventional rigid mechanism comprises rigid hinges that are utilized to associate the rigid links and make them move. Due to the storage of energy between joints, these mechanisms always need more output than input. Recent research suggests that using the flexure-based compliant mechanism instead of the traditional rigid mechanism can easily address the problems of assembly, friction and lubrication while also being lightweight, can improve the accuracy.

1.3. Project proposal

Based on the two directions discussed above, two models were proposed: one is the symmetric cross-spring pivot (CSP) and another is the asymmetric crossing four-bar linkage (FBL) with a flexural joint replacement, which is the highlight of this paper.

Besides the similar structure to the cruciate ligament, the same motion characteristics of center shift are also the reasons why this work chooses these two models. Centre shift is a kind of parasitic motion, an important kinematic phenomenon in mechanisms, which refers to some dependent motions that accompany other independent motions. It may introduce some undesired motion components which lead to lower manipulation accuracy/quality and more difficulties in calibration. On the other hand, it may perform a motion task by using a lower degree of freedom (DOF) PM that leads to a lower cost, lower complexity of kinematics and easier controls.[18] Thus, we should make the most of the characteristic of centre shift to mimic the knee motion.

On the other hand, the reference provided for the model design is vitally significant to ensure accuracy. We choose Guo's[19] model, a bio-joint formulated based on the characterization of the joint mechanics and musculoskeletal geometry as the reference dataset for the following design after reading a great deal of relevant paper.[19] He analysed the kinematic and dynamic of the bio joint from the aspect of the contact location between femur and tibia as well as the forces /torque acting on the knee, respectively, presenting the superiority of the bio-joint by comparing with the planar joint. The snapshots of the bio-joint shown in Fig. 3, and the dataset is from Guo[19].

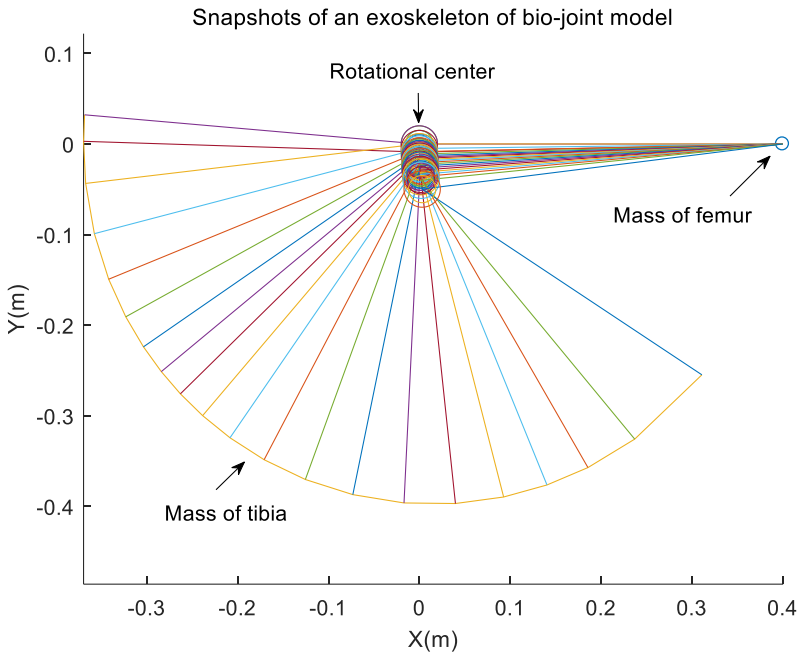


Figure 3 Snapshots of the bio-joint.[19]

The objective of the present paper is to design a lightweight, simple-structure, compliant mechanism for knee rehabilitation. To address the existing problems mentioned above, two models are proposed, cross-spring pivots and crossing four-bar linkage whose motion trajectory is similar to the human knee joint. The rest of this paper is organized as follows. In Section 2, the human knee biomechanics and kinesiology analysed according to its composition, moving trajectory and stress condition are presented. Then, the kinematics and kinetostatics analysis of cross-spring pivot and asymmetric crossing four-bar linkage are investigated through mathematical equations and figures in Section 3. In the next section, the model based on two models is simulated and optimized through theoretical and FEA results, comparing with bio-joint and choosing the best fit datum. In Section 5, the verification experiment is described. Results and conclusion are presented in Section 6.

2. Knee joint analysis

2.1. Complex function of the knee joint

The knee joint is composed of the medial tibiofemoral, the lateral tibiofemoral, the patellofemoral and the proximal tibiofibular joint. A few ligaments maintain the equilibrium of each direction to the knee joint. The anterior and posterior cruciate ligaments (ACL and PCL) attach the femur to the tibia crossly affecting the range of motion of the knee joint. The crossed four-bar linkage system and the Burmester curve were first proposed by Menschik as the basic element of knee kinematics in 1974 (Fig. 4a).[20] The ACL and PCL act as gears and the menisci with their capsular attachments as the power control and brake system, keeping the stability of the knee all together (Fig. 4b). The Burmester curve is also the most significant element used to repair and reconstruct the ligament, pain or injuries caused when the ligaments move beyond the ideal path of the curve.

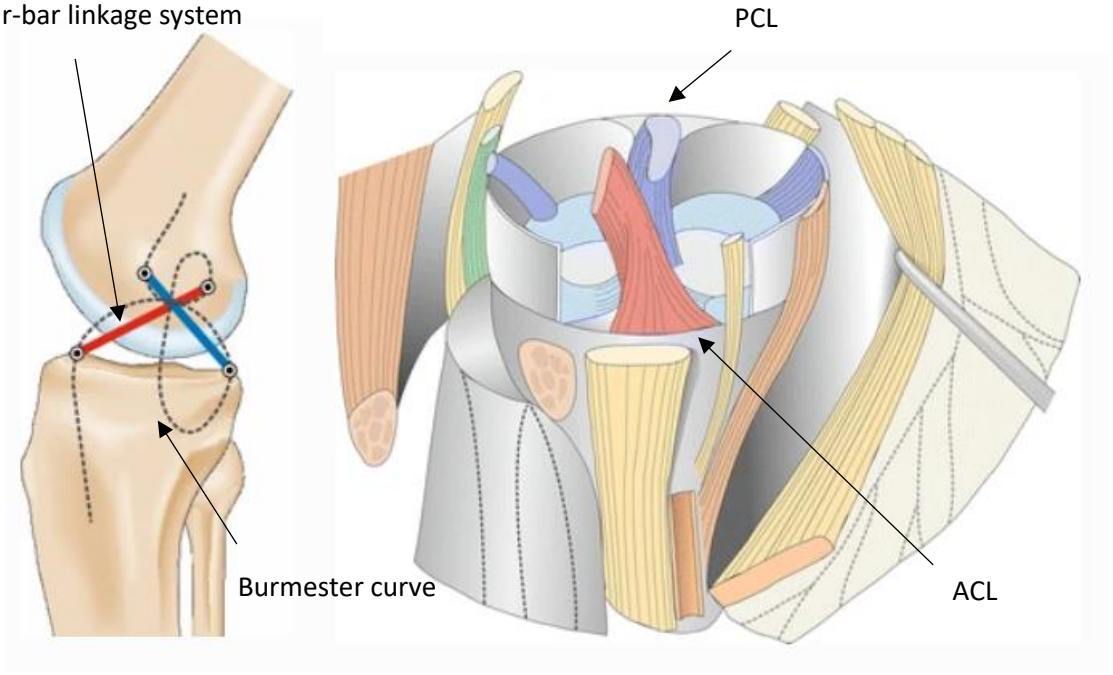


Figure 4 Four-bar linkage system: **a** Illustration of the Burmester curve and four-bar linkage system, and **b** Illustration of ACL and PCL with medial and lateral menisci.[21]

In our daily activities, knees take on a majority of our body weight, allowing a wide range of motion for flexion–extension and internal–external rotation. The knee joint is a trochoginglymos, meaning a gliding hinge joint. The main principle of knee joint kinematics

are rolling, gliding and rotation. The knee joint offers six degrees of freedom range of motion. The rotational movement consists of flexion–extension, internal–external and varus–valgus. The translational movement are possible in anterior–posterior and medial–lateral directions as well as by compression and distraction of the knee joint (Fig. 5). All these six freedoms of motion is in a combined complex function within the envelope of motion.[21]

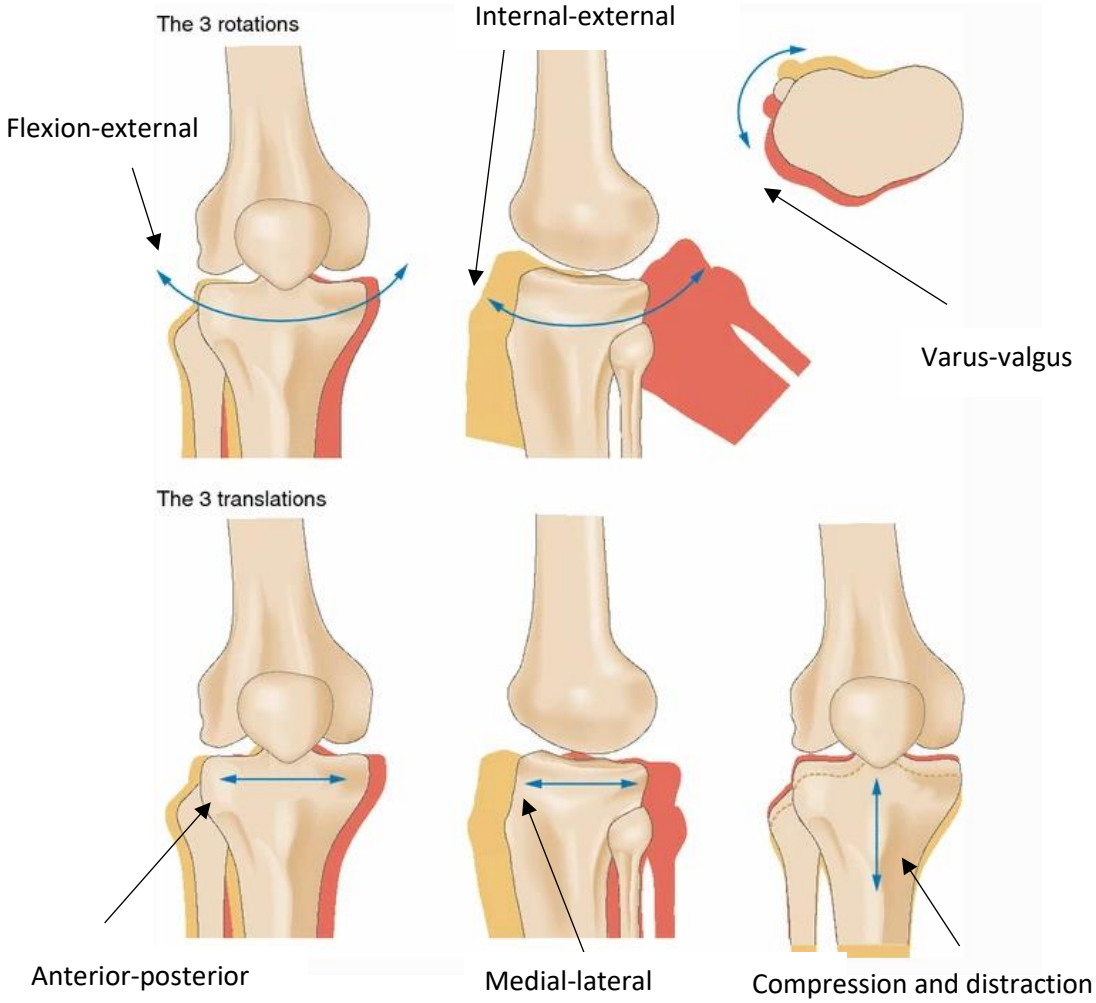


Figure 5 Knee joint has six degree of freedom for rotation and translation.[21]

To reduce the complexity, this work focuses only on the sagittal plane motion which is the main movement. In the sagittal plane, the combination of rolling and gliding are the main element shown in Fig. 6. It becomes easy to understand how the femoral condyle rolls (Fig. 6a), glides (b), and rolls and glides together (c) on the tibia.[22] Pure rolling or sliding will cause misalignment, which can cause a dysfunctionality of the joints. Moreover, it can be easily figured out that the real knee moves with a polycentric motion, which means the centre of rotation changes during rotation.

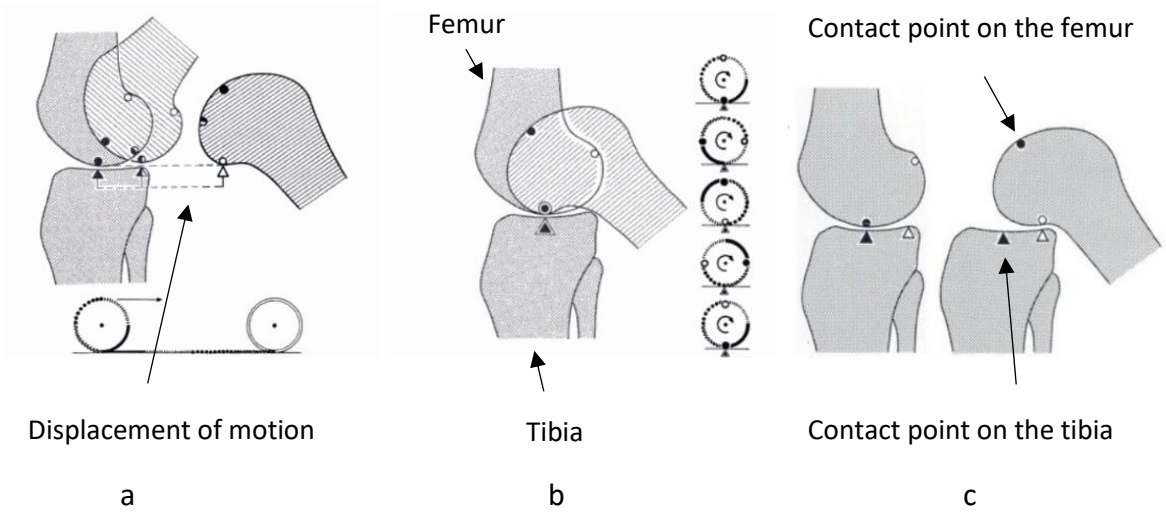


Figure 6 Movement of the femur relative to the tibia during flexion: **a** Pure rolling, **b** Pure gliding, **c** Combination of rolling and gliding.[22]

2.2. Sliding-rolling ratio

In the case of normal flexion or extension of the human knee joint, the local kinematics of the patellofemoral joint can be characterized as partial rolling and sliding.

With the electromagnetic techniques (MRI) (Iwaki et al., 2000[23]), the details of internal geometries of joints can be obtained and the S_{roll}/S_{slide} ratio of 1.7 is given by the kinematic models. In (Guo et al., 2010[19]), the S_{roll}/S_{slide} ratio is not a constant, but its average value of 1.69 closely consents to Iwaki's results plotted in Fig. 7 (the dataset from Guo[19]).

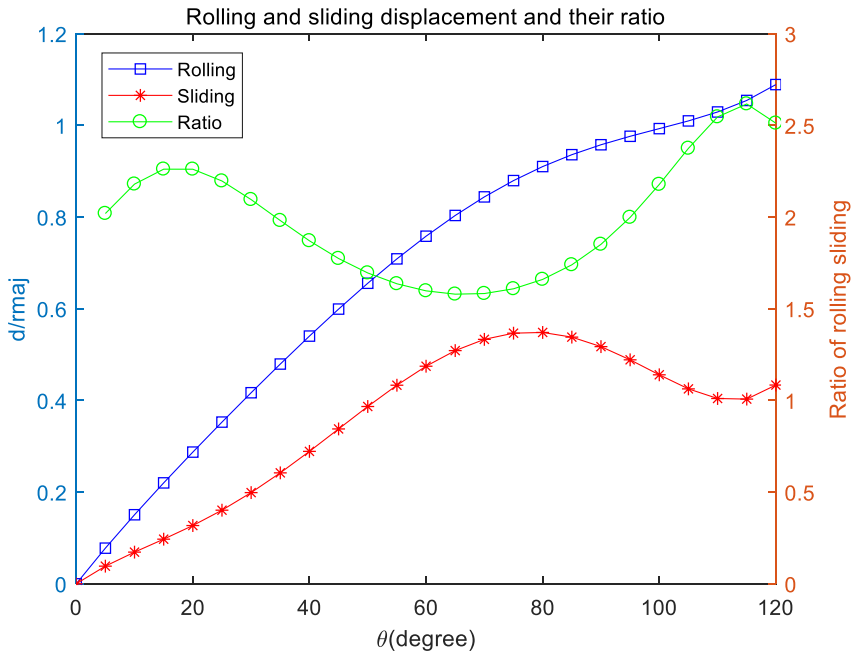


Figure 7 Plots of normalized rolling and sliding displacements.

The displacements, S_{roll}, S_{slide} are given by Eqs. (2-1) and (2-2), respectively, as a function of the flexion angle θ (the function from Guo[19]):

$$S_{roll}(\theta)/r_{maj} = 0.093\theta^5 - 0.409\theta^4 + 0.57\theta^3 - 0.448\theta^2 - 0.926\theta \quad (2\text{-}1)$$

$$S_{slide}(\theta)/r_{maj} = 0.334\theta^5 - 1.518\theta^4 + 2.12\theta^3 - 0.996\theta^2 + 0.513\theta \quad (2\text{-}2)$$

Where S_{roll}, S_{slide} are the displacement of the rolling and sliding, respectively; r_{maj} is the length of the major axis of the ellipse, assumed that the shape of the joint is elliptic.

In order to figure out the kinematic functions of the knee joint, we introduce the bio-joint proposed by Guo[19] to analyse the knee motion in depth.

2.3. Bio-joint analysis

Due to the kinematic constraint imposed by the contact, the human knee joint embodies two degrees of freedom (DoF) combination, rotation and translation for its planar motion. Guo[19] established a bio-joint (BJ) model based on anatomy and physiology which was chosen after comparing with the simple revolute (pin) joint. The motion trajectories of the mass center of femur and tibia, and the rotational centre of the knee joint shown in Fig. 8, which regards as the reference for the following design.

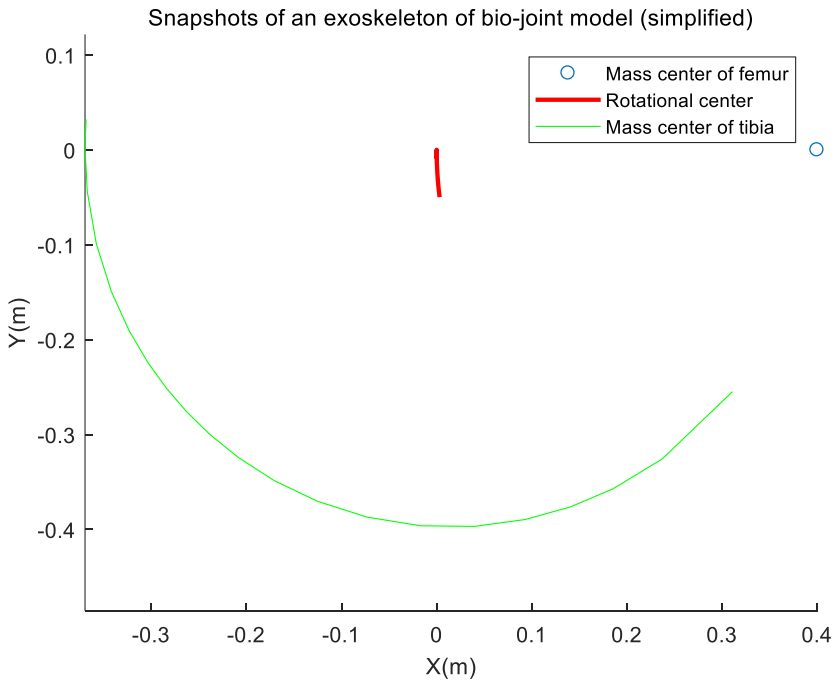


Figure 8 Snapshots of an exoskeleton of bio-joint model.

Numerical values used in this study are given in Table 2 (Nomiyama et al., 2007[24]).

Table 2 Physical parameters of human's lower leg.

	Human		**Exoskeletonlength (m)**
	Length (m)	Mass (kg)	Length (m)
Upper leg	0.40	7.02	0.40
Lower leg	0.37/0.27	2.44/1.18	0.37
$r_o\ (m)$	0.2453		

Fig. 8, the simple version of Fig. 3, shows the trajectory of the rotational centre (red bold line) and the tibia (green fine line), which illustrates the position of the rotational centre changing while rotation apparently. Note that the dataset is from Guo[19].

Then, we compared the displacements of the rotational centre (the orange line) and the mass centre of the tibia (the blue line) shown in Fig. 9, respectively, surprised to find out the displacements of the two lines are the same, which indicates that we can focus on the movement of the rotational centre when we investigate the kinematics of the human knee. Fig. 10**a** and **b** show the trajectory of the rotational centre, and its displacement, respectively.

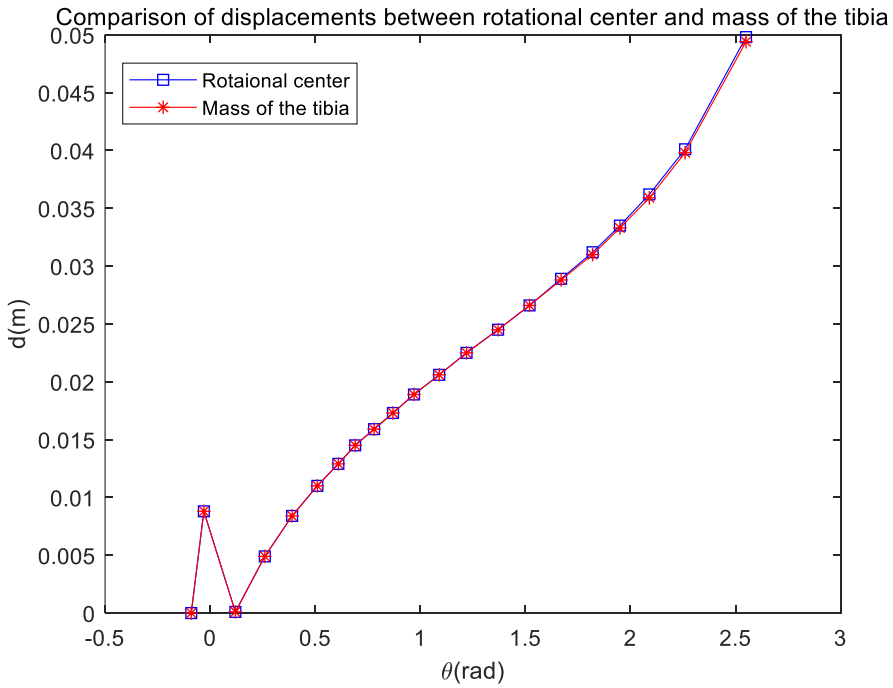
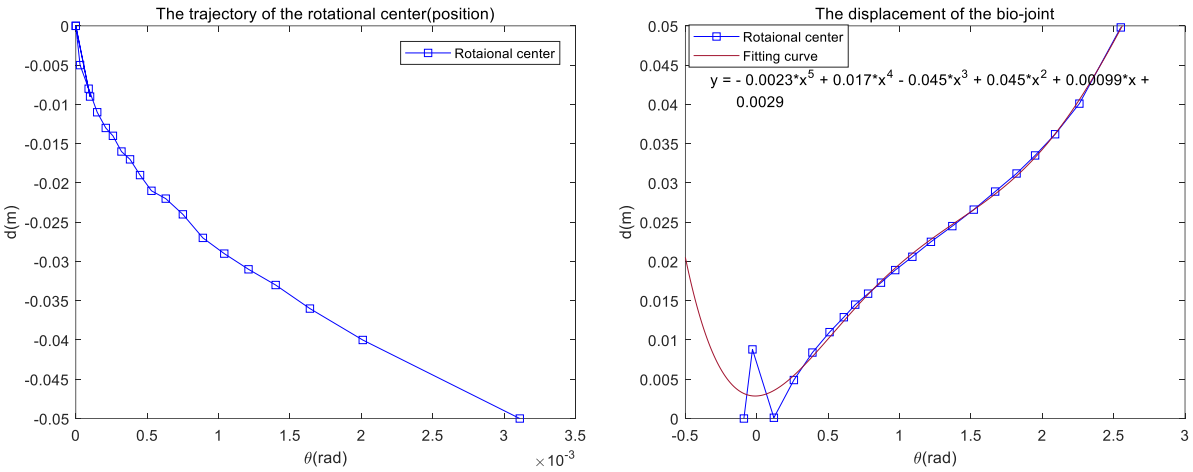


Figure 9 Comparison of displacements of centre point and end point.



a b

Figure 10 The rotational centre point of bio-joint: **a** The trajectory of bio-joint rotational centre, and **b** The displacement of bio-joint rotational centre.

Where Fig. 10**a** represents the position of the rotational centre point and Fig. 10**b** represents the displacement of the rotational centre point. The displacement of the rotational centre can be fitted to a function of rotational angle θ, as Eqs. (2-3):

$$d = -0.0023\theta^5 + 0.017\theta^4 - 0.045\theta^3 + 0.045\theta^2 + 0.00099\theta + 0.0029 \qquad (2\text{-}3)$$

The function given above is regarded as the reference utilized to optimize the models proposed in the next chapter, and the detailed analysis shown in Chapter 4.

3. Modeling of two compliant mechanisms

3.1. The generalized cross-spring pivot

Compliant mechanisms have been exploited extensively in the precision machine by taking advantage of centre shift as a parasitic motion. In terms of the advantages of its simple-structure, long-lasting and less-friction, a flexural pivot has a broader range of application than a conventional one. And the leaf-type flexural pivots as its high-capability of motion and uniform-distribution of stress attracts so many researchers devoting their life to investigate.[25] Hubbard et al constructed a novel fully compliant planar linear-motion mechanism which was combined by a set of compliant Roberts mechanisms in series and parallel.[26] A high precision butterfly flexible pivot was proposed in pointing and scanning space realizing both large motion range and small centre shift by Henein et al.[27]. To reduce the error from the parasitic motion, Zhao et al, utilized a high-accuracy linear-motion flexure mechanism with generalized cross-spring pivots based on a parasitic motion compensation approach, which not only predicted the stiffness and stress properties of the generalized cross-spring pivot but also revealed some useful characteristics.[28]

The cross-spring pivot, composed of two symmetric leaves intersecting at the midpoint, usually improve the characteristic of centre shift by changing the position of the cross point and the length of the leaves. Owing to the advantages of ease of assembly, maintenance-free, no backlash, diminished friction, infinitesimal resolution, and monolithic manufacturing, the flexural pivots are widely used in precision machines.

Although the cross-spring pivot has been applied in a wide range of areas where the conventional joint could not touch, the accuracy characteristics are still hard to be proved due to the internal geometry constraint and the elastic average of nonlinear mechanisms. Besides pure bending load, the payload also produced an effect on centre shift. However, adding the external force and moment on the pivot like Zelenika and DeBona[29], is not enough to get the properties of parasitic motions. The position of cross point also works proved by Wittrick.[30] On the other hand, the processing defects is a vital factor influence the accuracy characteristics investigated by Ryu and Gweon.[31] Thus, Zhao et al[32] established a non-dimensional model to derivate the accuracy characteristics of cross-spring pivot shown below.

3.1.1. The centre shift of the generalized cross-spring pivot

Since the behaviour of the cross-spring pivot is related to several transcendental equations, it is hard to understand the physical characteristic of the mechanism. Some accurate approximations are presented in order to offer better insight into the kinematics of the cross-spring pivot, including the definition of the parameters. All the formula calculated and derivate below are taken from Zhao.[33]

The lower-case letters are non-dimensional parameters. They are defined as:

$$m = \frac{ML}{EI}, \quad f = \frac{FL^2}{EI}, \quad p = \frac{PL^2}{EI}, \tag{3-1}$$

where M, F and P denote bending moment, tangential force, and axial force respectively; L, W and T are the length, width, and thickness of the beam respectively, and they are named as shape parameters, I is the moment of inertia; E is Young's modulus of the material. λ and α are deemed as the geometric parameters shown in Fig. 11 (a), which affects the accuracy of the mechanisms.[33]

1. Load-rotation relationships

When the typical external loads acting on the moving platform, the issue will be settled by considering the equilibrium condition of load and the compatibility of geometry.

The equilibrium condition of load can be written as:

$$(P_2 - P_1)sin\alpha + (F_1 + F_2)cos\alpha = F \tag{3-2}$$

$$(P_1 + P_2)cos\alpha + (F_1 - F_2)sin\alpha = P \tag{3-3}$$

$$(M_1 + M_2) + [(P_1 - P_2)cos\alpha + (F_1 + F_2)sin\alpha]\lambda Lsin\alpha cos\theta - [(P_1 + P_2)sin\alpha - (F_1 - F_2)cos\alpha]\lambda Lsin\alpha sin\theta = M \tag{3-4}$$

The compatibility of geometry is expressed as:

$$(\delta_{y1} - \delta_{y2})cos\alpha + (\delta_{z1} + \delta_{z2})sin\alpha = 2\lambda sin\alpha(1 - cos\theta) \tag{3-5}$$

$$(\delta_{y1} + \delta_{y2})sin\alpha - (\delta_{z1} - \delta_{z2})cos\alpha = 2\lambda sin\alpha sin\theta \tag{3-6}$$

Removed the higher-order terms, the expression of the load-rotation relationship is given as[33]:

$$\theta = \frac{15cos\alpha(\lambda f cos\alpha + m)}{(18\lambda^2 - 18\lambda + 15\lambda cos^2\alpha + 2)p + 120cos\alpha(3\lambda^2 - 3\lambda + 1)} \tag{3-7}$$

2. Centre shift of the generalized cross-spring pivot

Bonding the geometric considerations on the point B_1 and B_2 shown in Fig. 12 (b), the expressions of the centre shift are arranged as:

$$dx = -\frac{1}{cos\alpha}\left\{\frac{1}{150}(9\lambda^2 - 9\lambda + 1)(12\lambda - 1)\theta^3 + 6cot^2\alpha(2\lambda - 1)\left[\frac{\theta}{d} + \frac{1}{6300}(9\lambda^2 - 9\lambda + 11)\theta^3\right]\right\} - \frac{12\lambda - 1}{20sin^2\alpha}\left[\frac{\theta}{d} + \frac{1}{6300}(9\lambda^2 - 9\lambda + 11)\theta^3\right]p \tag{3-8}$$

$$dy = \frac{1}{2cos\alpha}\left\{\frac{-2}{15}(9\lambda^2 - 9\lambda + 1)\theta^2 + \frac{1}{1500}(2592\lambda^4 - 3024\lambda^3 + 1338\lambda^2 - 241\lambda + 2)\theta^4\right\} + \frac{1}{2cos^2\alpha}\left[\frac{1}{d} + \frac{1}{6300}(9\lambda^2 - 9\lambda + 11)\theta^2\right]p \tag{3-9}$$

Considering the horizontal force f performs equally as the bending moment m during rotation, thus, ignoring the role of horizontal force f. Significantly, the centre shift will be the minimum when the following condition is satisfied Eq (3-10), hence when$\lambda = (3 \pm \sqrt{5})/6$ the generalized will rotate at the smallest parasitic motion.

$$9\lambda^2 - 9\lambda + 1 = 0 \tag{3-10}$$

The Eqs. (3-8) and (3-9) cannot guarantee the accuracy when the geometric parameter λ is greater than 0.5, which is beyond the previous assumptions adopted to simplify the problem. When λ is greater than 0.5, the λ' will be $1 - \lambda$, after satisfying the boundary and initial condition the equations of the centre shift can be rewritten as:

$$dx = \frac{1}{cos\alpha}\left\{\frac{1}{150}(9\lambda^2 - 9\lambda + 1)(12\lambda - 1)\theta^3 + 6cot^2\alpha(1 - 2\lambda)\left[\frac{\theta}{d} + \frac{1}{6300}(9\lambda^2 - 9\lambda + 11)\theta^3\right]\right\} + \left[\frac{(11 - 12\lambda)}{20}\left(\frac{1}{sin^2\alpha} + \frac{\theta^2}{cos^2\alpha}\right) - \frac{1}{2}\left(\frac{1}{sin^2\alpha} - \frac{1}{cos^2\alpha}\right)\right]\left[\frac{\theta}{d} + \frac{1}{6300}(9\lambda^2 - 9\lambda + 11)\theta^3\right]p \tag{3-11}$$

$$dy = \frac{-1}{15cos\alpha}(9\lambda^2 - 9\lambda + 1)\theta^2 + \frac{1}{cos\alpha}\left[\frac{1}{3000}(2592\lambda^4 - 5184\lambda^3 + 3678\lambda^2 - 1511\lambda + 447) - \frac{cot^2\alpha(1 - 2\lambda)}{1050}(9\lambda^2 - 9\lambda + 11)\right]\theta^4 + \left[\frac{(11 - 12\lambda)}{20}\left(\frac{1}{cos^2\alpha} - \frac{1}{sin^2\alpha}\right)\theta^2 + \frac{1}{2}\left(\frac{\theta^2}{sin^2\alpha} + \frac{1}{cos^2\alpha}\right)\right]\left[\frac{1}{d} + \frac{1}{6300}(9\lambda^2 - 9\lambda + 11)\theta^2\right]p \tag{3-12}$$

$$d = \sqrt{dx^2 + dy^2} \tag{3-13}$$

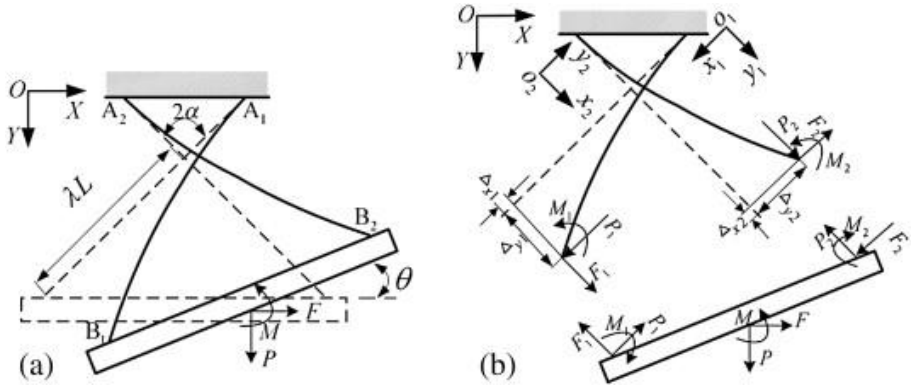


Figure 11 The relationships between loads and displacements for a generalized cross-spring pivot: **(a)** A deflected generalized cross-spring pivot, and **(b)** The exploded view for the loads and displacements.[33]

In summary, the centre shift of the generalized cross-spring pivot can be calculated via Eqs. (3-8), (3-9), (3-11), (3-12). The displacement of centre shift d can be obtained by Eq. (3-13).

3.1.2. Accuracy analysis of the generalized cross-spring pivot

According to the formulas shown above, it is tempting to conclude that the geometric parameters λ and α, external loads p are the factors of the accuracy, while the machining defects are also the effects. The detailed discussions of these influence will be analysed as following which are summarized from Zhao.[33]

1. Geometric parameters λ and α

The geometric parameters λ and α influence both components, dx and dy, of the center shift strongly. As the figures shown in Zhao,[33] when the rotational angle is 15 degree and the geometric parameter λ is 0.8, the displacement on the X-axis, dx, will change from positive to negative, which is beneficial for the compensation of the parasitic motion. In terms of the displacement on the Y-axis, dy, it is symmetric about horizontal axis λ equal to 0.5, and when $\lambda = 12.7322\%$ or 87.2678%, dy is zero. Meanwhile, the dimensions of dy increases with the increasing α.

2. Vertical force p

The vertical force p influences the centre shift by changing the rotational stiffness. When the rotational angle is fixed, the p has little impact on centre shift. However, when $\lambda =$

12.7322% or 87.2678%, the center shift (especially for dy) influenced dramatically by p, leading to the zero value of centre shift. What's more, the influence of p plays the same role on λ and $1-\lambda$, a condition of the inverse moving platform.

3. The machining defects

The parasitic motion also influenced by processing imperfections, such as the shape parameters L, W, T, geometric parameter α, and the errors induced by leaf offset. While the errors caused by machining can be avoided through choosing the appropriate processing technology which is not summarized here.

3.2. The crossed four-bar linkage

3.2.1. Four-bar linkage

Four-bar mechanisms are the simplest closed-chain linkage which consists of four rigid bodies connected in a loop by four joints. Not only planar four-bar linkages, spherical and spatial four-bar linkages also exist and are used in practice. Generally, the links move in parallel planes, and there are three basic styles depending on the use of revolute or prismatic joints: four revolute joints, three revolute joints and a prismatic joint, two revolute joints and two prismatic joints. In addition, the planar quadrilateral linkages (4R) are important mechanisms found in machines and can be designed to guide a wide variety of movements. One of the typical types of planar quadrilateral linkages is the crossing linkage whose two links cross over each other.

As the proposal mentioned, the structure and characteristic of the crossing four-bar linkage are similar to the cruciate ligament of the human knee joint, and considering a compliant mechanism is suitable for wearable devices. Therefore, we analyse the kinematics of the rigid crossing four-bar linkage firstly, then replace the rigid hinges with flexural hinges.

3.2.2. Kinematics of rigid four-bar linkage

Due to the cruciate ligament is an asymmetric crossing four-bar linkage, the geometrical relationship has some differences from the generalized four-bar linkage. To simplify the calculation, we introduce a model shown in Fig. 13 proposed by Karami et al. [34], which is exactly the simulation for the human knee joint.

The mechanism is coupler-link driven whose mobility needs to be discussed in details. The triangle inequality concept was utilized to define the mobility conditions for four-bar linkages and provided a graphical interpretation to mobility determination by Midha et al.[35] A unified method of mobility analysis based on the concept of linkage discriminant was proposed by Angeles and Bernier.[36] For the coupler-driven linkage, two driving methods are supposed to be. One is driven by an external force and another is external torque. Obviously, the second method fits the situation. To realize the crossed four-bar linkage, inequality (3-14) becomes the Grashof criterion, while inequality (3-15) is satisfied too. (Fig. 12)[37]

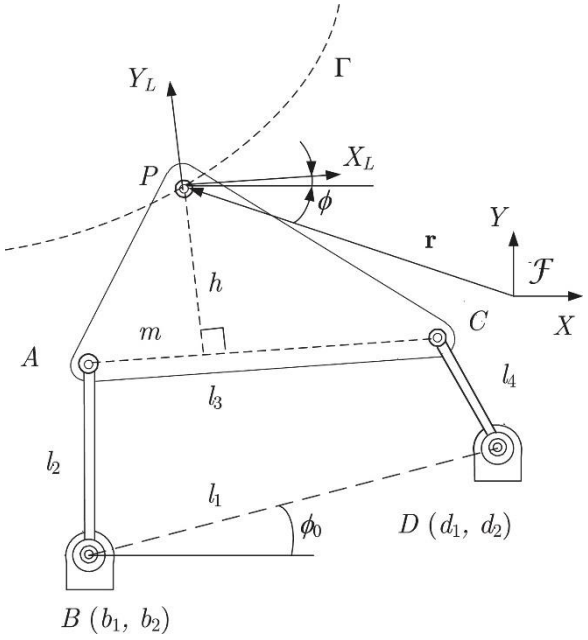


Figure 12 A coupler-driven four-bar linkage.[37]

$$l_1 + l_3 < l_2 + l_4 \tag{3-14}$$

$$(l_1 - l_3)^2 > (l_2 + l_4)^2 \tag{3-15}$$

Line AD is fixed and the angle $\varphi_1$is known. Line BC is the moving platform determined by the rotational angle φ_3. We regard AD as femur and BC as tibia of the knee. The length of AD, AB, BC, CD are known and denoted by r_1, r_2, r_3, r_4, respectively. The angle φ_2 and φ_4 can be expressed by the function that depends on the angle φ_3 shown as follows.

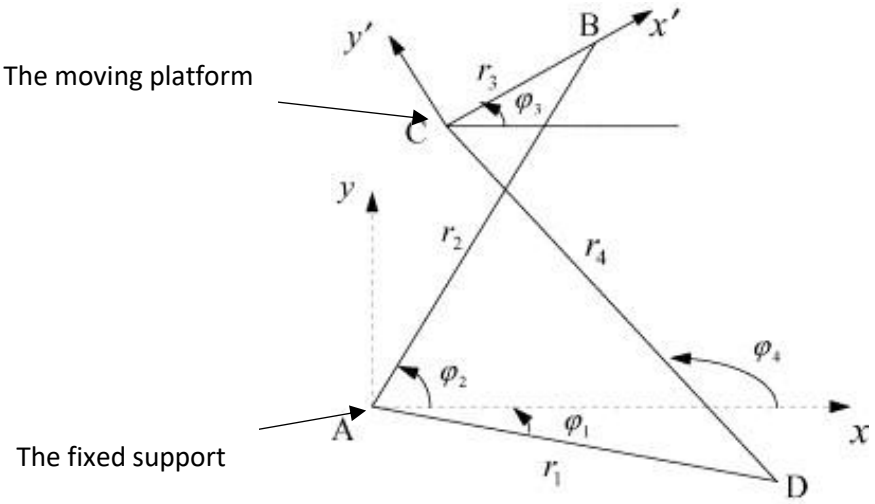


Figure 13 The model of the asymmetric crossing four-bar linkage.[34]

From the geometric relation and by considering A (x_A, y_A), B (x_B, y_B), C (x_C, y_C), D (x_D, y_D), we have:

$$x_C = x_D + r_4\cos(\varphi_4) = x_A + r_2\cos(\varphi_2) + r_3\cos(\varphi_3) \tag{3-16}$$

$$y_C = y_D + r_4\sin(\varphi_4) = y_A + r_2\sin(\varphi_2) + r_3\sin(\varphi_3) \tag{3-17}$$

By considering:

$$C_1 = x_D - x_A - r_3\cos(\varphi_3) \tag{3-18}$$

$$C_2 = y_D - y_A - r_3\sin(\varphi_3) \tag{3-19}$$

We have:

$$r_2\cos(\varphi_2) = r_4\cos(\varphi_4) + C_1$$

$$r_2\sin(\varphi_2) = r_4\sin(\varphi_4) + C_2$$

We pose:

$$E = 2C_2r_4$$

$$F = 2C_1r_4$$

$$G = r_2^2 - r_4^2 - C_1^2 - C_2^2$$

We obtain:

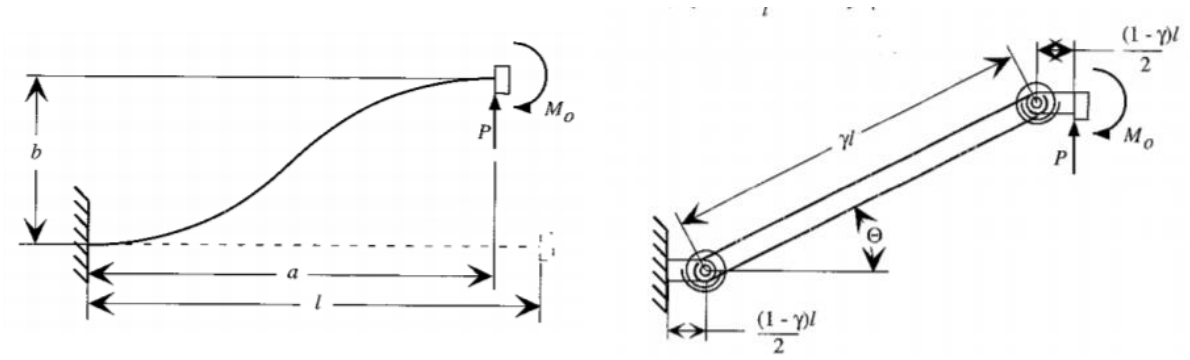
$$E\sin(\varphi_4) + F\cos(\varphi_4) = G \tag{3-20}$$

Using Eq. (3-20), we can find the angle of φ_4, then with the Eq. (3-16) to (3-19), we can find the angle of φ_2 and the coordinates of point C. Knowing the coordinates of point A, B, C, D, the coordinate of rotational centre O can be calculated.

3.2.3. The flexural hinges replacement of the crossing four-bar linkage

Following the current research, we replace the rigid joints with flexural joints, which is lightweight and reduces the difficulties of assembly widely used in mechanisms. While the kinematic analysis of the compliant mechanism is complex and difficult, thus, we describe the motion and the force of a compliant mechanism using a rigid-body mechanism with equivalent behaviour, the Pseudo-Rigid-Body Model (PRBM).

Considering the two crossed hinges join the fixed and moving platforms, respectively, the same situation to the fixed-guided flexible segment with one end of the beam is fixed while the other is guided in that angle of that end of the beam (Fig. 14a and b). Thus, the springs add on each connection shown in Fig. 15.



a b

Figure 14 The fixed-guided flexible segment: **a** Flexible beam, and **b** Pseudo-Rigid-Body Model.[38]

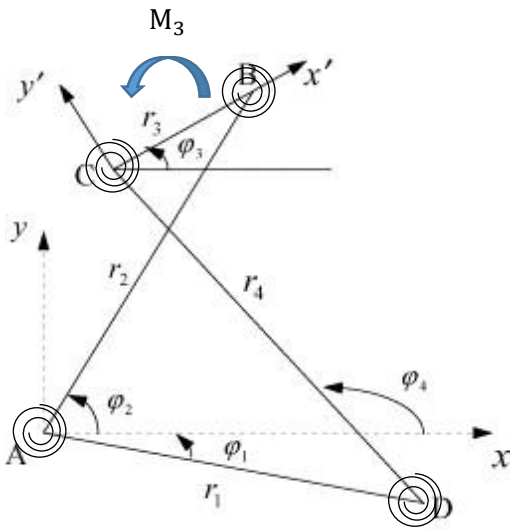


Figure 15 The model of the asymmetric crossing four-bar linkage (with moment).[34]

1. Stiffness analysis

The replaced flexural hinges are treated as the fixed-guided beams which have four torsional springs (as R joints) as shown in Fig. 15. The stiffness and location of each torsional spring are obtained from the PRBM as reported in[38]:

$$K_i = 2\gamma K_\Theta \left(\frac{EI}{l}\right)_i \tag{3-21}$$

Where $K_\Theta = 2.67617$ is the stiffness coefficient; $\gamma = 0.8517$ signifies the characteristic radius factor; $i = 1,2,3,4$ represents the four springs; E is Young's modulus; $I = \frac{WT^3}{12}$ (W is the width and T is the thickness) is the moment of inertia of the cross-section hinges; and L is the length of the identical flexural hinges. The numerical values of γ, K_Θ are found from the Table 5.1 in Howell[38] with the determined factors n and ϕ.

2. Kinetostatic analysis

To obtain the relationship between input load and output displacement, the virtual work principle is introduced as required.

1) The principle of virtual work.

Virtual work is the total work done by the external and inertial forces of the mechanical system as it moves through a set of virtual displacements, which has always been used in the study of statics. When considering loads exerted to a body in static equilibrium, the principle

of least action requires the virtual work of these forces to be zero, known as the principle of virtual work. This principle can be generalized such that three-dimensional rotations are included: the virtual work of the applied force and applied moments is zero for all virtual movements of the system from static equilibrium.

2) Application of the principle of virtual work

For the crossing four-bar linkage, we only apply a moment M_3on the moving platform, as shown in Fig. 15. The Moment-rotation relationship derived yields according to Howell[38]:

The total virtual work for this system is performed as follows:

$$W = Ah_{23} + B + Ch_{43} = 0 \tag{3-22}$$

Where

$$A = (T_1 + T_2)h_{23}$$

$$B = M_3 - T_2 - T_3$$

$$C = (T_3 + T_4)h_{43}$$

The value of the moment T_i is

$$T_i = -K_i\Psi_i \ (i = 1,2,3,4)$$

The Lagrangian coordinates for the joints are

$$\Psi_1 = (\varphi_2 - \varphi_{20})$$

$$\Psi_2 = (\varphi_2 - \varphi_{20}) - (\varphi_3 - \varphi_{30})$$

$$\Psi_3 = (\varphi_4 - \varphi_{40}) - (\varphi_3 - \varphi_{30})$$

$$\Psi_4 = (\varphi_4 - \varphi_{40})$$

Where φ_i , $(i = 1,2,3,4)$ defines the position of the mechanism when the springs are undeflected, and $\varphi_{i0} = \varphi_i$ at its initial position.

The values of the kinematic coefficients are

$$h_{23} = \frac{\delta\theta_2}{\delta\theta_3} = \frac{r_3 \sin(\varphi_3 - \varphi_4)}{r_2 \sin(\varphi_4 - \varphi_2)}, h_{43} = \frac{\delta\theta_4}{\delta\theta_3} = \frac{r_3 \sin(\varphi_3 - \varphi_2)}{r_4 \sin(\varphi_4 - \varphi_2)}$$

Finally, the relationship between moment and rotation is rewritten from Eq. (3-22)

$$(T_1 + T_2)h_{23} + M_3 - T_2 - T_3 + (T_3 + T_4)h_{43} = 0 \quad (3\text{-}23)$$

The complete derivation is referenced from Howell.[38]

4. Mechanisms optimization

4.1. Cross-spring pivot

Based on Zhao's[33] results, the geometric parameters λ and α are the main factors that influence cross-spring pivot parasitic motion. Meanwhile, the vertical force p also affects the centre shift by rotational stiffness. Therefore, to optimize the cross-spring pivot canter shift and get closer to the bio-joint centre shift curve, we optimize the parameters λ and α, adding vertical force to adjust the stiffness.

4.1.1. The optimization methods

1. Theoretical optimization

The aim is to find the optimal parameters of cross-spring pivot such that the displacement of rotational centre describes a curve as close as possible to the curve obtained by the bio-joint. After consulting a great deal of literature, we utilize the least sum of difference method to get the best fit.

The steps are given as follows: first change one variable which are geometric parameters λ, α and the vertical force p given by Eqs. (3-8), (3-9), (3-11), (3-12) at a time; getting the displacements of the rotational centre of the cross-spring pivot $csp_{_d}$; then add up the differences comparing with bio-joint centre shift under different rotational angles (diffsum); finally comparing their sum of difference and choosing the minimum. (Fig. 16) It takes about 20 to 30 times when it reaches a minimum parameter. The parameters are optimized from the local to the whole. In general, it is a for loop programmed by Matlab. The example of λ optimization is shown in Fig. 16 and the detailed codes are shown in Appendices 8.1.

2. FEA optimization

As the modelling analysis illustrated, the centre shift of the model will be verified in FEA, which will be discussed in detail below. We will also adjust the parameters finely one variable at a time with the same method as the theoretical methods. Overall, the optimal parameters are achieved synthetically

.

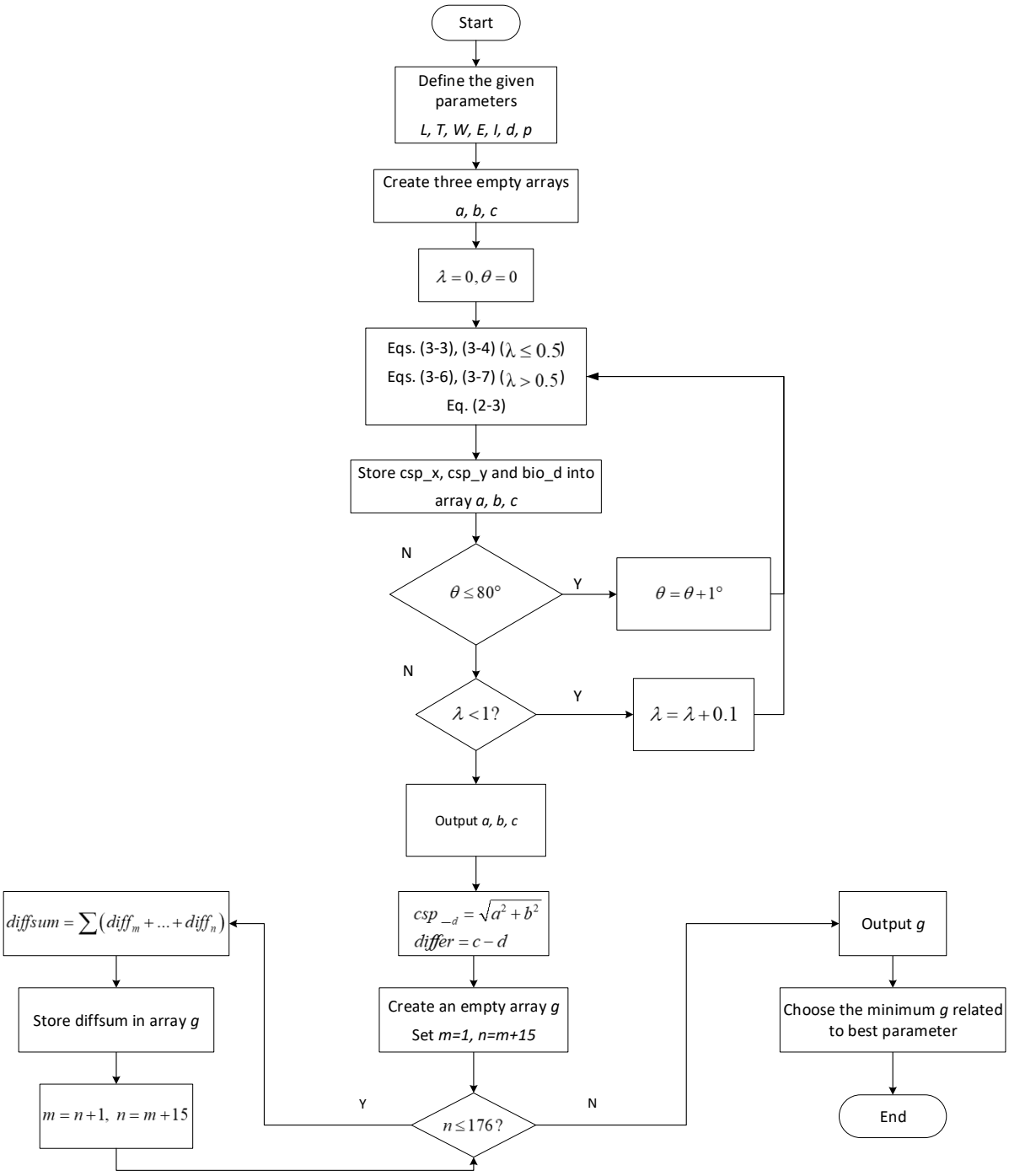


Figure 16 The logic flowchart of the optimization (cross-spring pivot).

4.1.2. FEA simulation

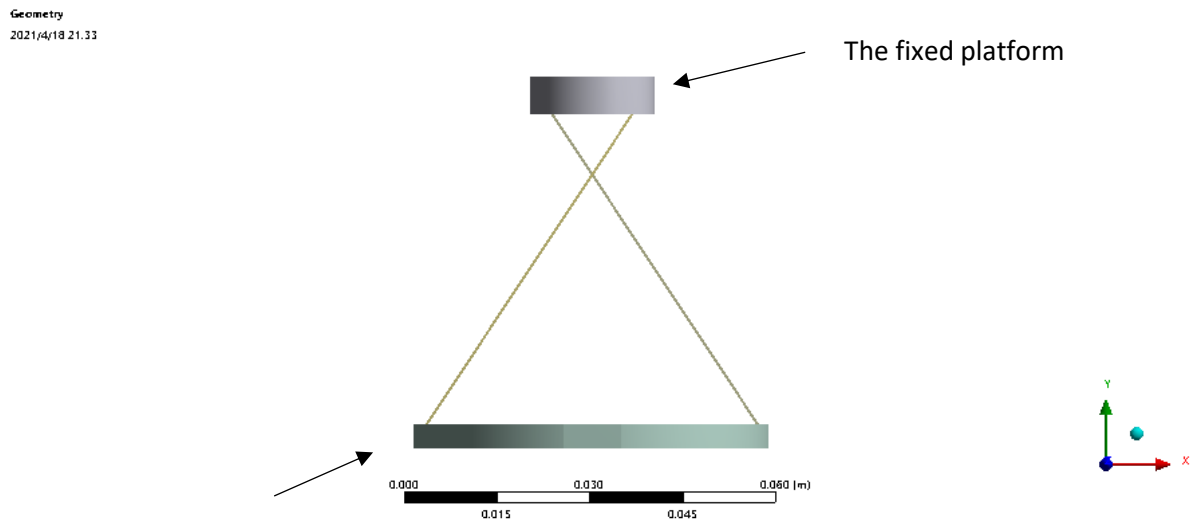
1. Simulation setting

To verify the analytical model as well as to confirm the performance of the model, a specific design as a case study was simulated in Comsol 5.0 (COMSOL Inc., Stockholm, Sweden). The material of the compliant leaves adopts beryllium bronze (the material parameters shown in

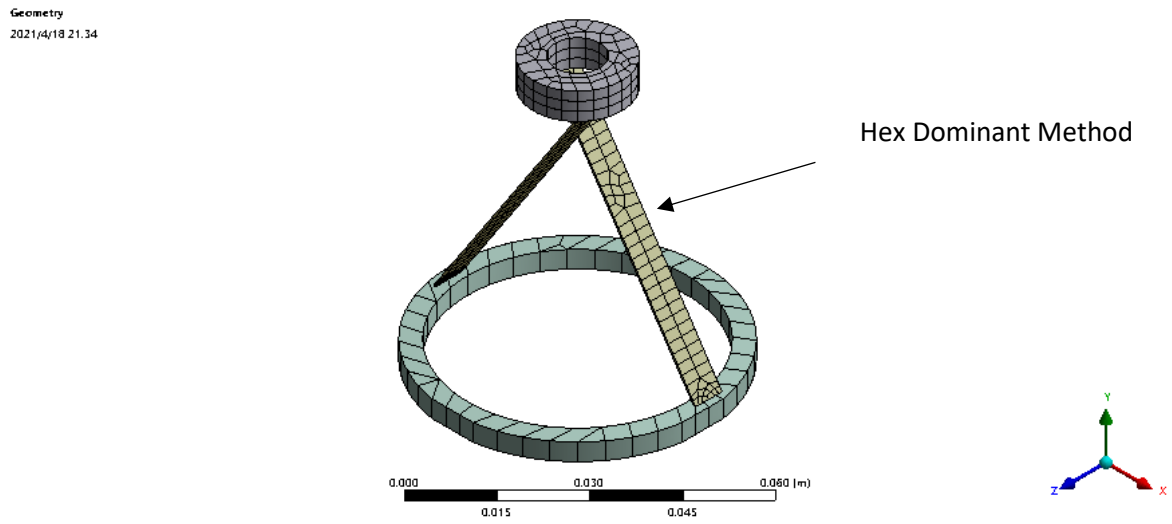
Table 3), and the platforms are considered as a rigid body. The grid division of the leaves is completed using the Hex Dominant Method to obtain the more precise solution (Fig. 17 b). The simulation was conducted by applying a remote displacement and an axial force on the lower platform, while setting a fixed support on the upper platform. The rotational angles are divided into 12 steps from 0 degree to 60 degrees acting on the moving platform, and the axial force is a constant value of 10 (*N*). The model and the deformed results are shown in Fig. 17a and Fig. 17c. When the moving platform rotates 60 degrees without force, the maximal of the total deformation is 0.051578 (*m*), and the maximal of the total deformation is 0.051669 (*m*) when adding force which occurs at both ends of the moving platform.

Table 3 The material parameters of beryllium bronze.

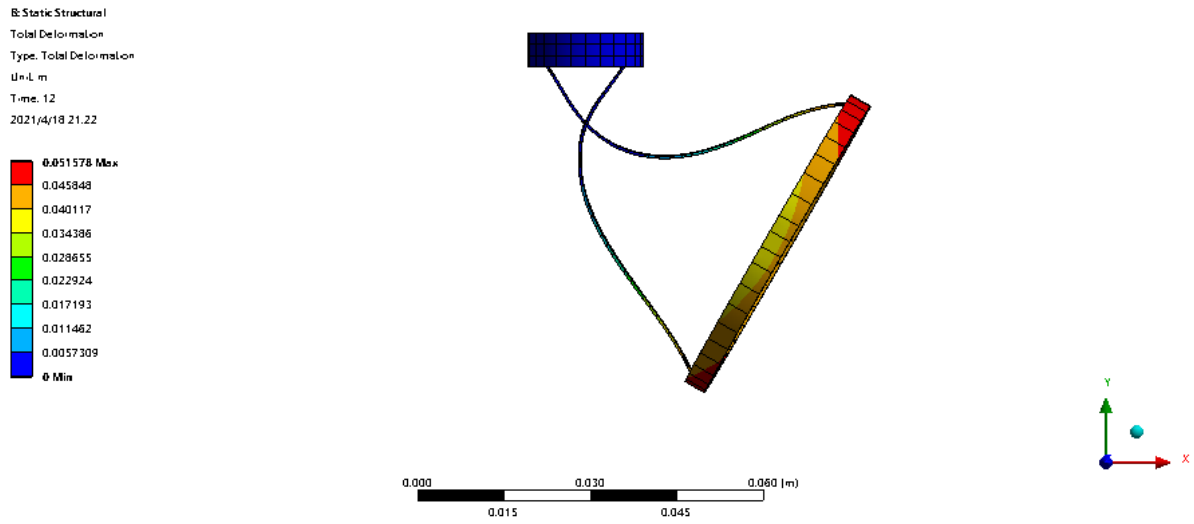
Modulus of elasticity (N/m^2)	Poisson's ratio	Density (kg/m^3)
1.25E+11	0.300	8.25E+03



a



b



c

Figure 17 FEA simulation (cross-spring pivot): **a** Front view of the model, **b** Hex Dominant Meshing, **c** Simulation demonstration.

2. Data processing

Since the rotational centre point is changing during rotation, we cannot capture the centre point during FEA. Thus, we catch the position of endpoints A_1 and A_2 of the fixed platform (Fig. 18) and calculate the displacement of the rotational centre O' according to the following geometric relationship.

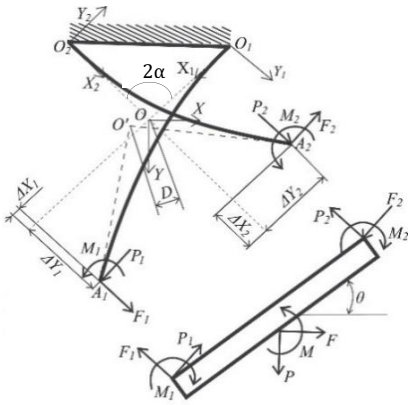


Figure 18 The geometric relationship between endpoints A_1, A_2 and rotational centre O′.[39]

$$\begin{cases} X = x_{A1} + sin\,(\alpha - \theta) \cdot \lambda L \\ Y = y_{A1} + cos\,(\alpha - \theta) \cdot \lambda L \end{cases} \tag{4-1}$$

$$\begin{cases} X = x_{A2} - sin\,(\alpha + \theta) \cdot \lambda L \\ Y = y_{A2} + cos\,(\alpha + \theta) \cdot \lambda L \end{cases} \tag{4-2}$$

Where X, Y are the coordinates of the rotational centre on the X-axis and Y-axis, respectively. Then, we will get the displacement of the rotational centre easily.

A detailed comparison of centre shift among FEA analytical, theoretical calculation and bio-joint will be discussed in 4.1.3.

4.1.3. Comparison

1. The optimization results

The optimization results are shown in Fig. 19 to 22, which demonstrate the displacement of centre shift under theoretical calculation, FEA solution and whether adding axial force on the model, comparing them with the bio-joint. The optimal parameters are listed in Table 4:

Table 4 The value of optimized parameters (cross-spring pivot).

Parameter	α(degree)	λ	p
Value	33.6	0.803	-0.58

2. Comparison between bio-joint and cross-spring pivot (without p)

The optimal parameters (without p) are substituted in Table 4 into Eqs. (3-11) to (3-13), and we obtain the displacements of the centre shift of cross-spring pivot, comparing the results with the bio-joint shown in Fig. 19. Then, arrange and calculate the datum from FEA solution as mentioned, the comparison between bio-joint and FEA results are shown in Fig. 20.

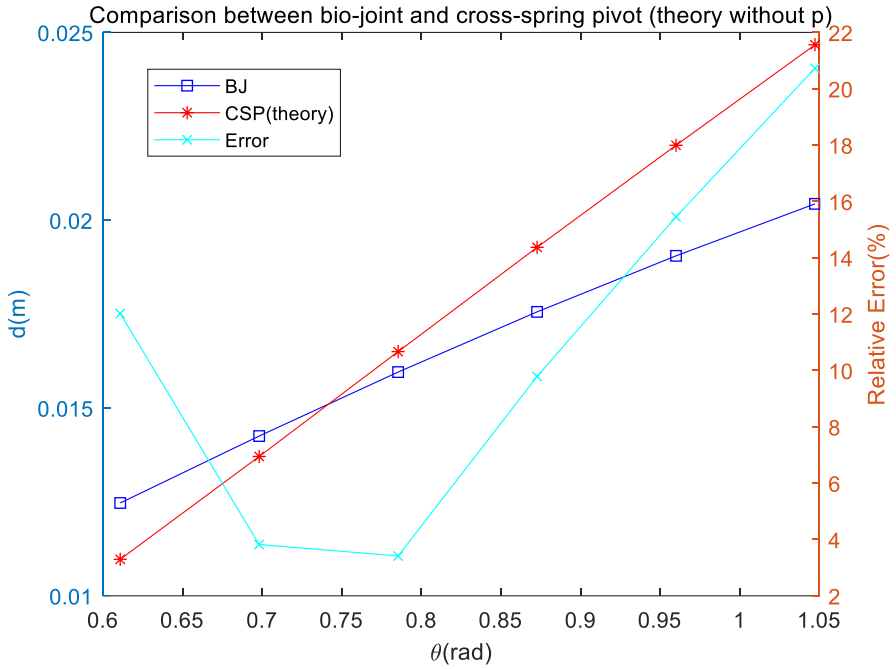


Figure 19 The comparison between bio-joint and cross-spring pivot (theoretical results without p).

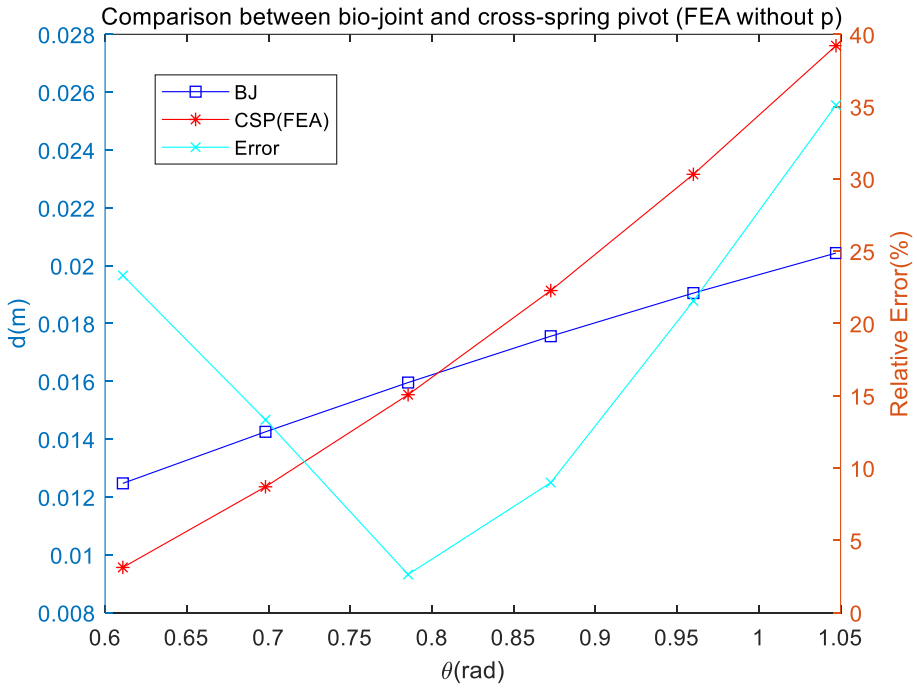


Figure 20 The comparison between bio-joint and cross-spring pivot (FEA results without p).

The relationship between displacement and rotation is graphically described in Fig. 19 which demonstrates a good agreement between theoretical results and bio-joint. The maximum relative error between theory and bio-joint is about 22 percent. Fig. 20 illustrates the relationship between displacement and rotation. There is more deviation of displacement

between FEA results and bio-joint than theory, which is about 40 percent difference. In addition, the plots also demonstrate the nearly linear relationship between displacement and rotation. As the rotation increases, the displacement of the centre shift increases.

3. Comparison between bio-joint and cross-spring pivot (with p)

To reduce the rotational stiffness of the model, add an axial force p to adjust it, which also affects the centre shift to some extent. Substitute all the optimal parameters in Table 4 into Eqs. (3-11) to (3-13), and the displacement of the centre shift will be obtained. The comparison between bio-joint and cross-spring pivot of theory is shown in Fig. 21. Then, follow the data processing to organize the FEA solution, comparing them with the bio-joint in Fig. 22.

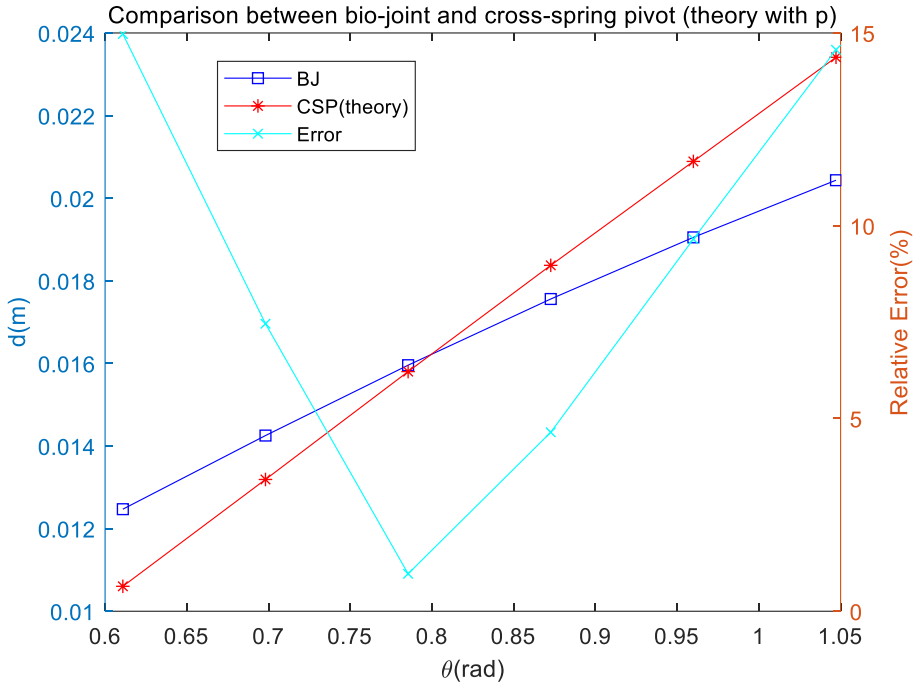


Figure 21 The comparison between bio-joint and cross-spring pivot (theoretical results with p).

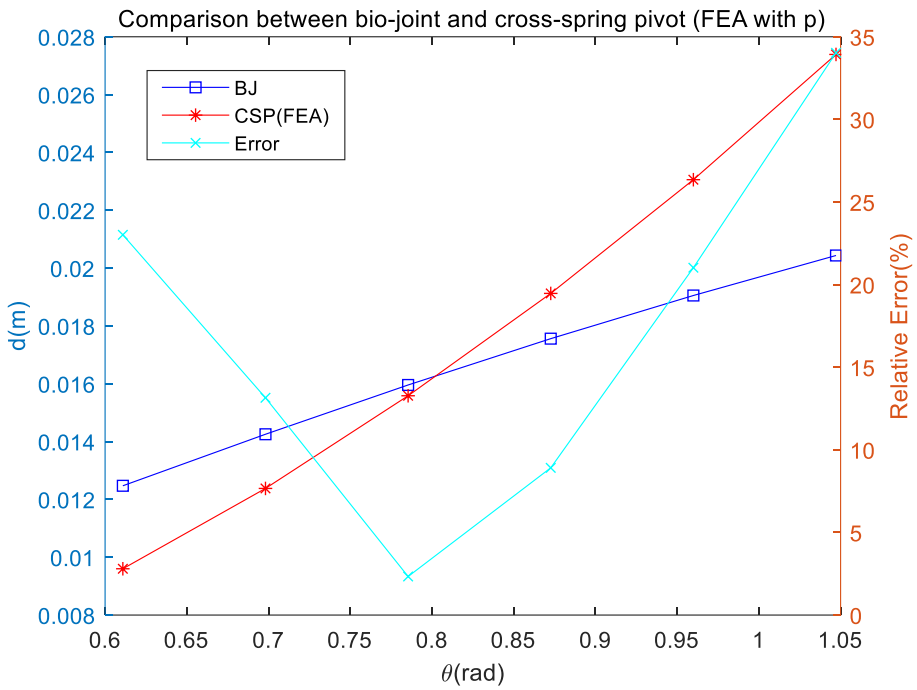


Figure 22 The comparison between bio-joint and cross-spring pivot (FEA results with p).

Fig. 21 demonstrates the relation between displacement and rotation with adding force through the theoretical calculation. We can observe that the theoretical results with p is better to match the bio-joint than ones without p, the maximum error of which is about 15 percent difference. While the FEA solution is more than double the theoretical results, which is 35 percent difference.

Considering the deviation between FEA and theoretical results, the undefined parameters might be one of the causes, such as the width and thickness of the platforms, which could be addressed by adjusting the parameters. Besides, the grid division might influence the accuracy of the solution, and changing the method works.

4.2. Crossing four-bar linkage

Previous analysis provides a good indication of the lengths of four links r_1, r_2, r_3, r_4 with the deflection angle of fixed platform φ_1 affecting the centre shift. Therefore, the optimization of crossing four-bar linkage will revolve around the five parameters to match the bio-joint curve.

4.2.1. The optimization methods

1. Theoretical optimization (rigid body)

We obtain the value of φ_2 and φ_4 according to Eqs. (3-16) to (3-20), and the positions of each point can also be obtained as well. The rotational centre of rigid four-bar linkage is the intersection point of line AB and line CD. Thus, the position and the displacement d of the rotational centre can be also known. After that, we use the similar method as 4.1.1, changing the geometric parameters $r_1, r_2, r_3, r_4, \varphi_1$, and comparing the difference between bio-joint and rigid four-bar linkage under different rotational angle (φ_3). Note that each parameter is changed in turn, summing up the group of datum in different rotational angle, and then compare the sums under the changing data. Finally, a minimum set of data is chosen, optimizing from local to global. The calculation is achieved by Matlab, the logic flowchart shown in Fig. 23 and the detailed programming listed in Appendices 8.2 (changing parameter φ_1 as an example).

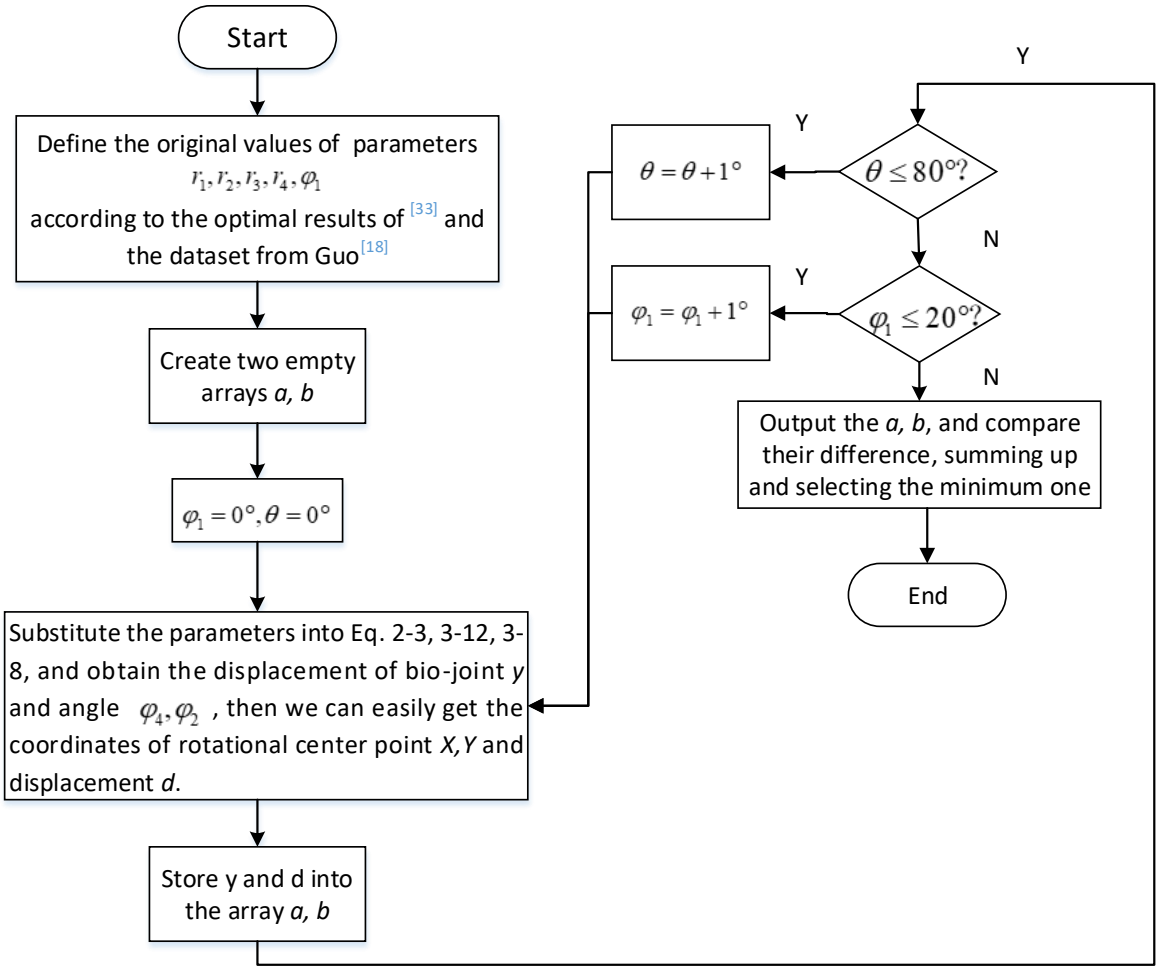


Figure 23 The logic flowchart of the optimization (crossing four-bar linkage).

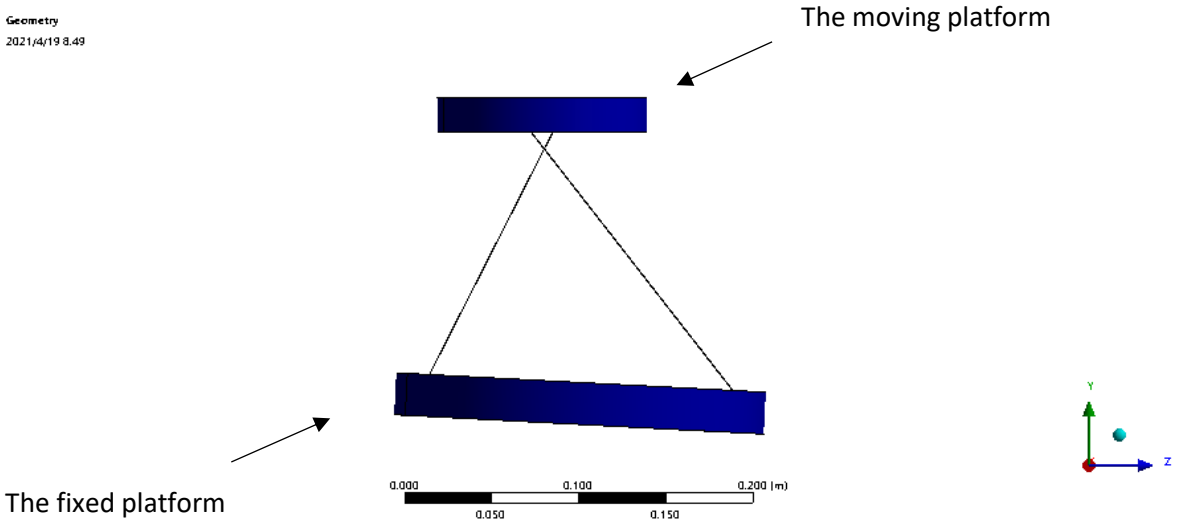
2. Flexural hinges replacement

Considering the adaptability and portability, the rigid hinges are replaced with flexural ones, which is the innovative point of this thesis. Modelling and simulating the model, compare the displacement of centre shift between rigid bodies, flexural linkage and the bio-joint, the details discussed below.

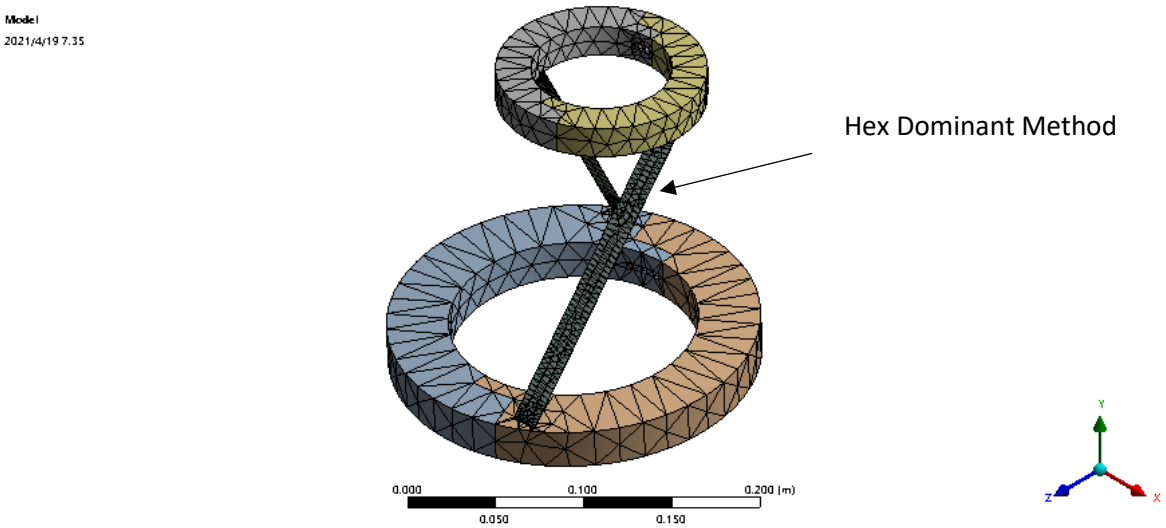
4.2.2. FEA simulation

1. Simulation setting

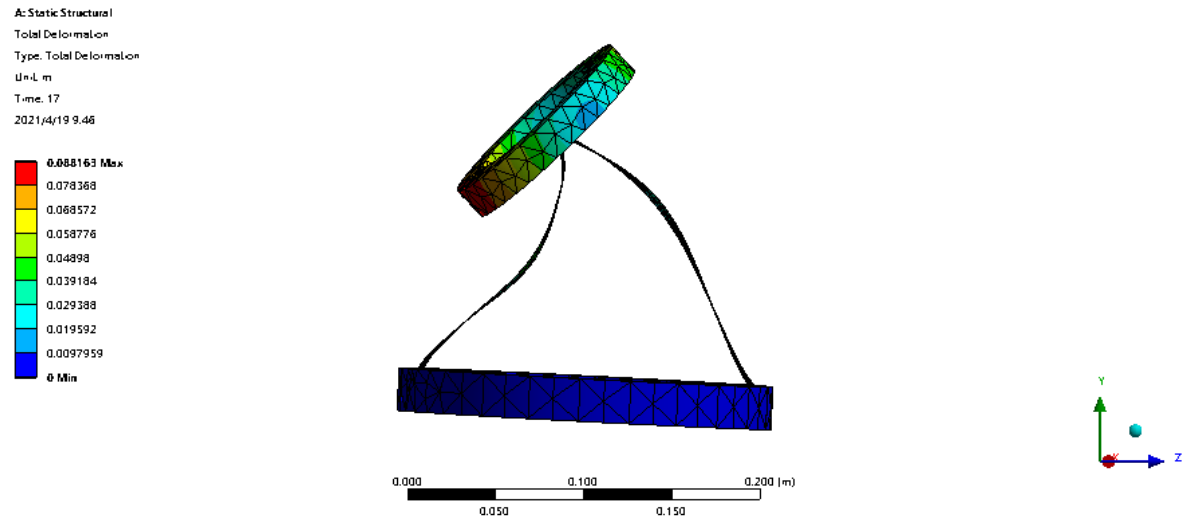
Before comparison, the FEA was conducted to obtain its corresponding performance according to Comsol 5.0 (COMSOL Inc., Stocklom, Sweden). The flexural hinges are made of beryllium bronze as well. The four-bar linkage adopts Hex Dominant meshing for the crossed bars and the initial setting for other parts shown in Fig. 24b. The simulation was guided by applying a remote displacement as well as an axial force on the upper platform while setting fixed support on the lower one. The rotational angles are divided into 12 steps from 0 degrees to 60 degrees adding on the moving platform. The maximum deflection, 0.088163 (m), occurs at the left side of the moving platform when it rotates 60 degrees, indicated in Fig. 24c, which increases as the rotational angle rises. With the remote displacement of 60 degrees, the moment reaction is -1.2418e+006 ($N \cdot m$). The detailed performances (i.e., the relationship between displacement and rotation and the correlation between moment and rotation) of the flexural four-bar linkage will be studied in 4.2.3 with quantitative comparisons among the FEA, theoretical results and bio-joint curve.



a



b



c

Figure 24 FEA simulation (flexural four-bar linkage): **a** Front view of the model, **b** Hex Dominant Meshing, **c** Simulation demonstration.

2. Data processing

It should be noted that the deformation obtained from the FEA solution is the displacement of both end points of the moving platform while the displacement of the rotational centre is unmeasurable. Furthermore, the initial positions of the four endpoints can be captured by the software. As the positions of the rotational centre are the intersection of the crossed bars which follow the functions below, the displacement can be obtained as well.

$$a_1 = \frac{y_A - y_B}{x_A - x_B}, \qquad b_1 = \frac{x_A \cdot y_B - x_B \cdot y_A}{x_A - x_B}$$

$$a_2 = \frac{y_C - y_D}{x_C - x_D}, \qquad b_2 = \frac{x_C \cdot y_D - x_D \cdot y_C}{x_C - x_D}$$

$$\mathrm{X} = -\frac{b_1 - b_2}{a_1 - a_2}, \qquad \mathrm{Y} = \frac{a_1 \cdot b_2 - a_2 \cdot b_1}{a_1 - a_2} \tag{4-3}$$

where (x_A, y_A), (x_B, y_B), (x_C, y_C), (x_D, y_D) are the positions of points A, B, C, D (Fig. 13), and X, Y are the coordinates of the rotational centre on the X-axis and Y-axis, respectively.

4.2.3. Comparison

1. The optimization results

Based on the optimization methods above, the values of lengths of four links r_1, r_2, r_3, r_4 and the angle of the fixed platform φ_1 are listed in Table 5.

Table 5 The values of optimized parameters (four-bar linkage).

Parameter	r1(m)	r2(m)	r3(m)	r4(m)	φ_1(degree)
value	0.174	0.158	0.022	0.2	3

2. Displacement-rotation relationship comparison between bio-joint and four-bar linkage

By substituting the optimal parameters in Table 5 into Eqs. (3-16) to (3-20), and the geometric relationship of four points will be obtained. Then, the displacement of the rotational centre can be easily gotten as well, comparing the theoretical results with the bio-joint shown in Fig. 25. Then, the FEA results are organized, comparing the difference with the bio-joint performed in Fig. 26.

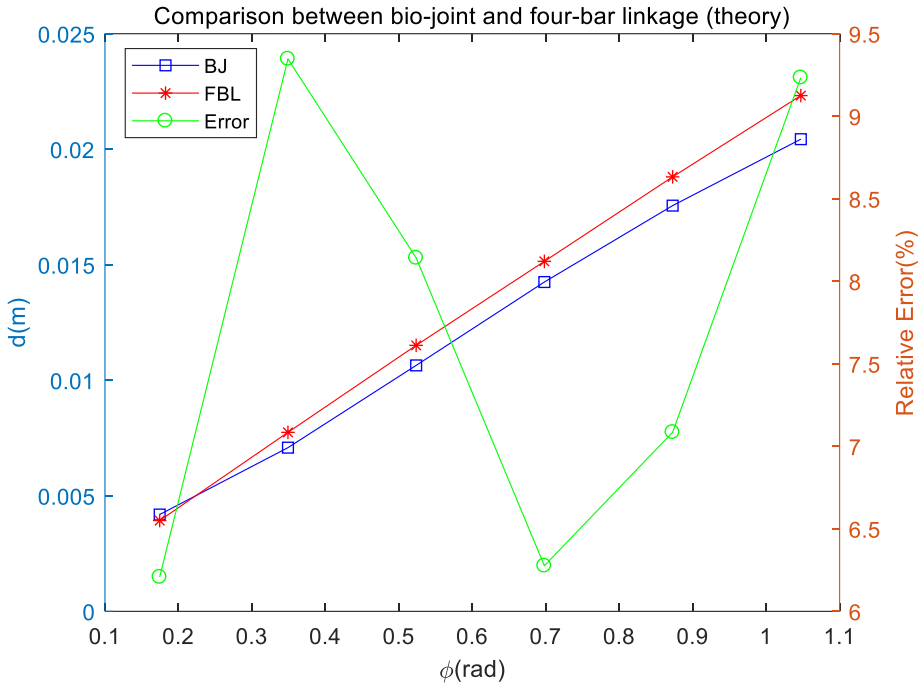


Figure 25 The comparison between bio-joint and four-bar linkage (theoretical results of the rigid joints).

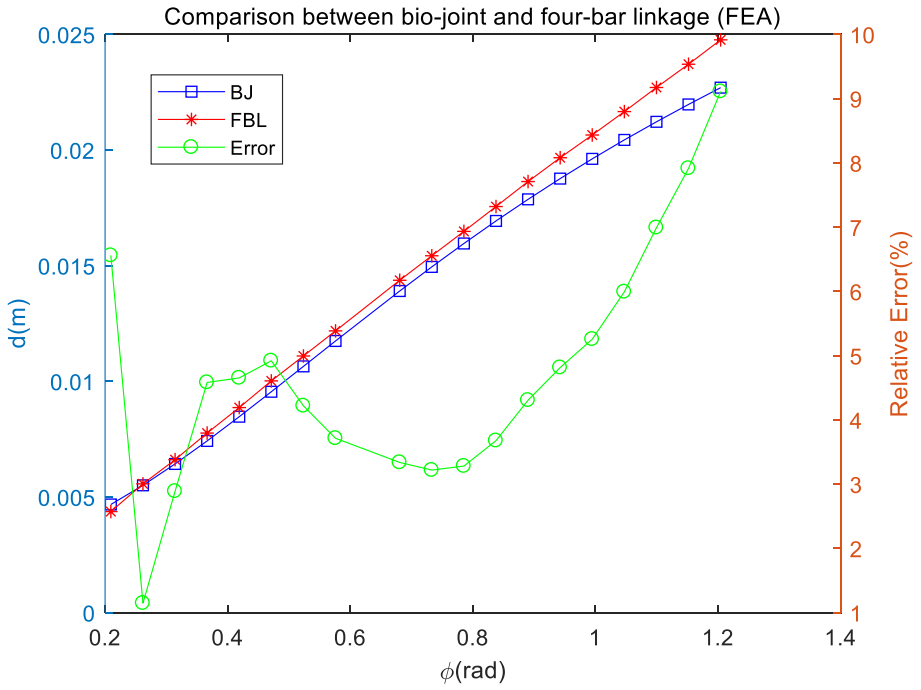


Figure 26 The comparison between bio-joint and four-bar linkage (FEA results of flexural joints).

Fig. 25 compares the displacement of the centre shift among the models obtained from rigid four-bar linkage theoretical results and bio-joint, which increase with the rotation. The largest deviation can be seen between theoretical results and bio-joint with a maximum difference

of about 9.5 percent, which verifies the accuracy of the optimization. Fig. 26 illustrates the comparisons of the flexural four-bar linkage between FEA results and bio-joint. The plot suggests a good agreement between FEA results and bio-joint with about 10 percent difference.

It is noticeable that the errors of FEA results are larger than theory slightly, which may be due to the appropriate method used to grid division and time step definition. The accuracy of modelling might be another factor of the error. To address these problems, checking the modelling before FEA and adjusting the meshing and analysis setting may work.

3. Moment-rotation relationship comparison between four-bar linkage and FEA results

Considering the kinetostatic analysis of the flexural four-bar linkage discussed in the last chapter, we utilize the derivation arranged in Eq. (3-22) to address the Moment-rotation relationship. Substituting the geometric parameters into the functions and solving in FEA software, we obtain the two curves of the Moment-Rotation shown in Fig. 27.

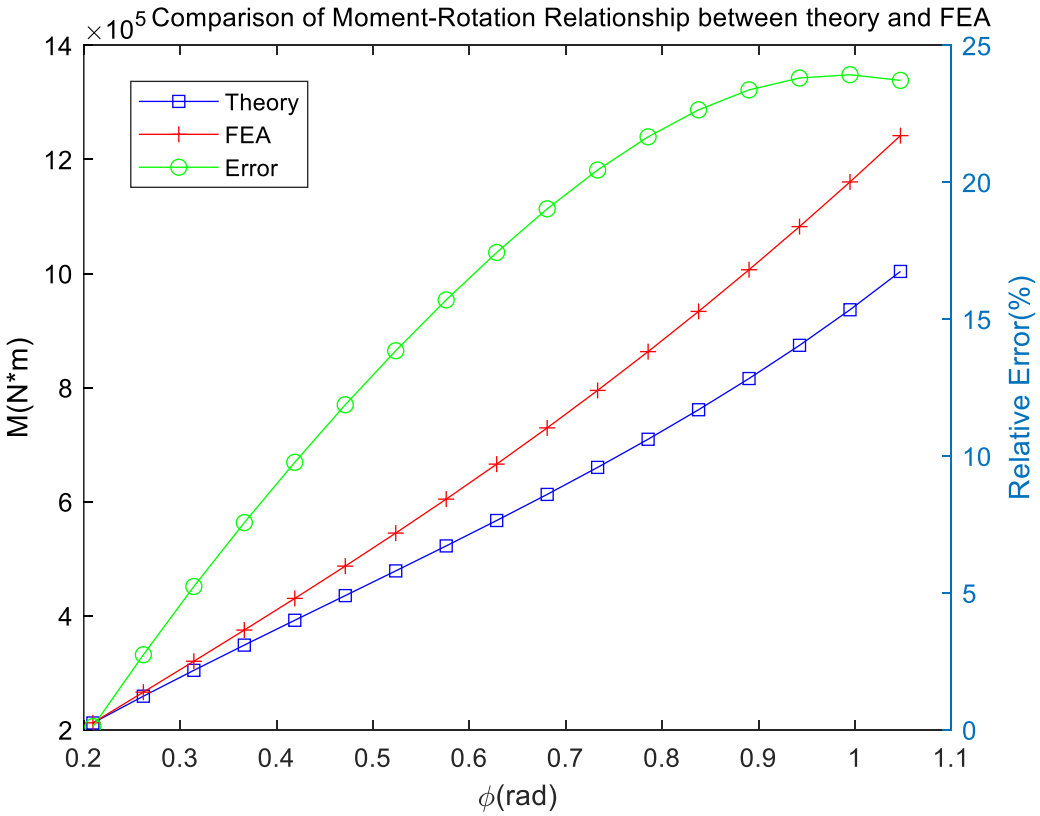


Figure 27 The comparison between FEA results and virtual work calculation (the moment-rotation relationship).

In Fig. 27, the FEA results show a steady increase of the displacement as the rotational angle rises and it ends at a maximum value of about 1.2×10^6 $(N \cdot m)$; while, the theoretical results follow the same trend with a small fluctuation. The difference between two results increases gradually, while the maximum difference is about 24 percent on 60 degrees, and the minimum difference is about 0 percent on 10 degrees.

The reason why it happens might due to the inaccuracy of the modelling or the simulation setting. According to optimizing the connected methods, adjusting the deviation between platforms and bars, ensure the inclining angle between platform and horizontal plane is the same as the theoretical value. To maintain the accuracy of the FEA simulation, changing the meshing methods and the connection methods, find out the most suitable setting of solution which also improves the accuracy.

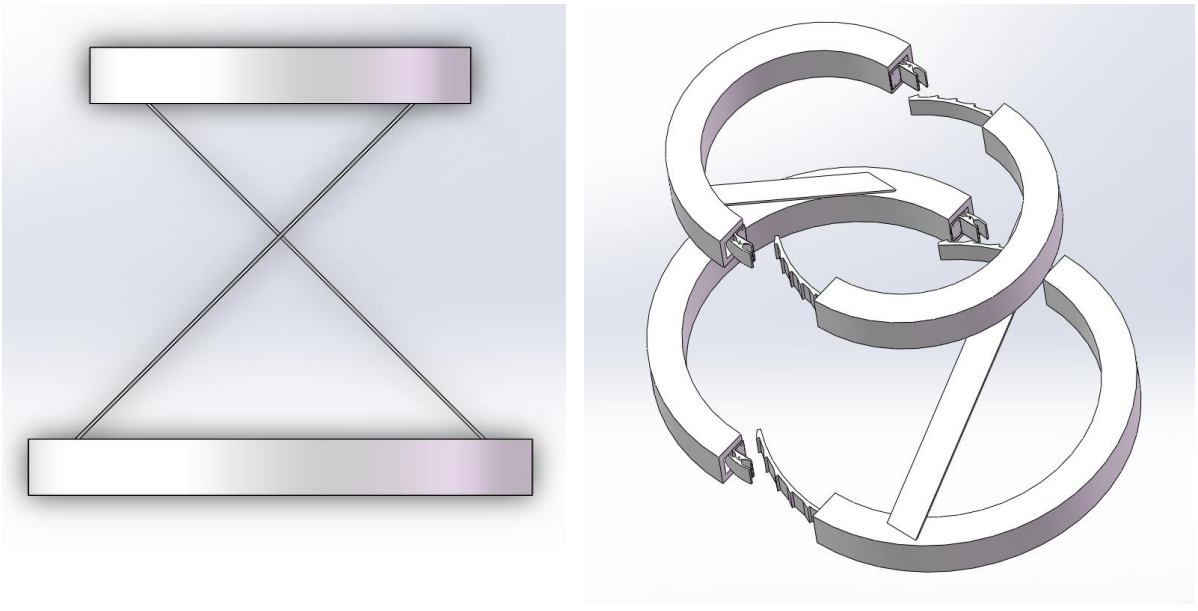
5. Prototype design and testing

This project aims to design a prototype and fabricate it to do the test. According to the optimization results above, we can easily obtain the geometric parameters which can be utilized for design directly. Two prototypes are proposed in 5.1 and 5.2 based on two models mentioned before: the symmetric cross-spring pivot and asymmetric crossing four-bar linkage with flexural hinges replacement.

5.1. Mechanism design

5.1.1. Mechanism design based on cross-spring pivot

The mechanism consists of two rings with two flexural shells that crossed connect. The big and small rings wear on the femur and tibia of the knee joint, respectively. The shells insert in the slots of the ring platforms, while the connection of the rings is inspired by the concept of roller skate laces, which can be adjusted freely, adapted to different circumferences of legs. The assembly drawing and the details of the connection are shown in Fig. 28 and Fig. 29.



a b

Figure 28 The assembly drawing of the cross-spring pivot model: **a** Front view, and **b** Isometric view.

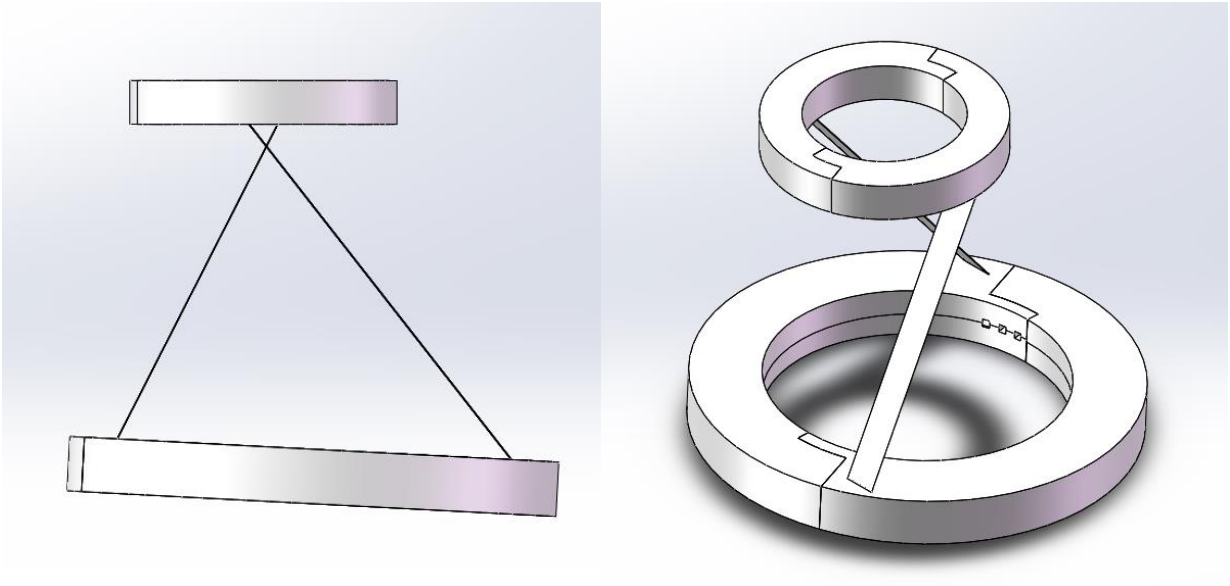


Figure 29 Adjustable laces inspiration.

Considering the creativity and accuracy, we do not adopt this prototype based on the cross-spring pivot. The mechanism proposed as follows is going to be fabricated.

5.1.2. Mechanism design based on crossing four-bar linkage

The device is composed of two rings with two flexural shells as well, and the shells are also inserted into the slots on the two rings. The connection between each half rings can be adjusted by inserting the different slot on the side of the rings. Furthermore, the big and small rings correspond to the femur and tibia of the knee joint, respectively. The assembly drawing and the details of the connection of rings are shown in Fig. 30 and Fig. 31.



a b

Figure 30 The assembly drawing of the crossing four-bar model: **a** Front view, and **b** Isometric view.

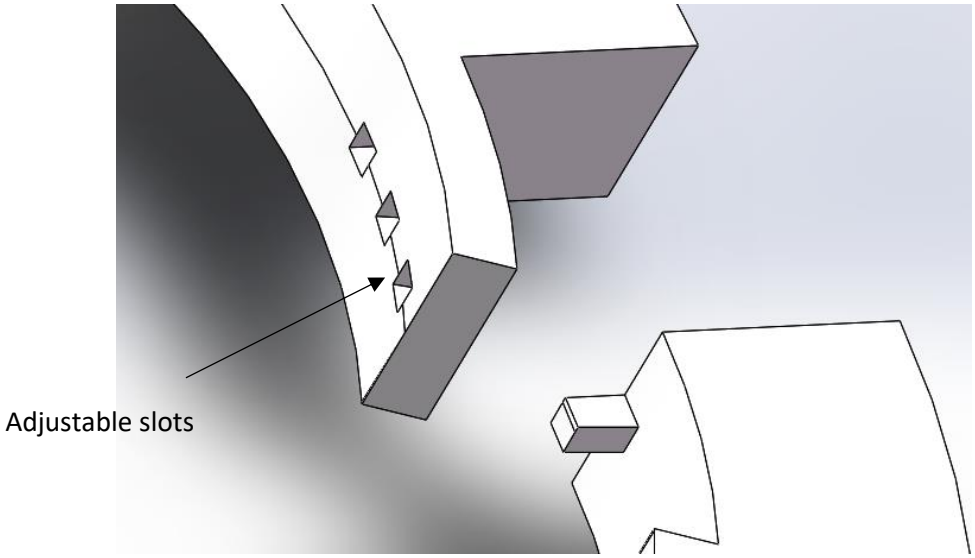


Figure 31 The details of the connection.

Due to the lower error between the crossing four-bar linkage and bio-joint, the design above is utilized to fabricate the prototype and do the test.

5.2. Fabrication and testing

5.2.1. Fabrication

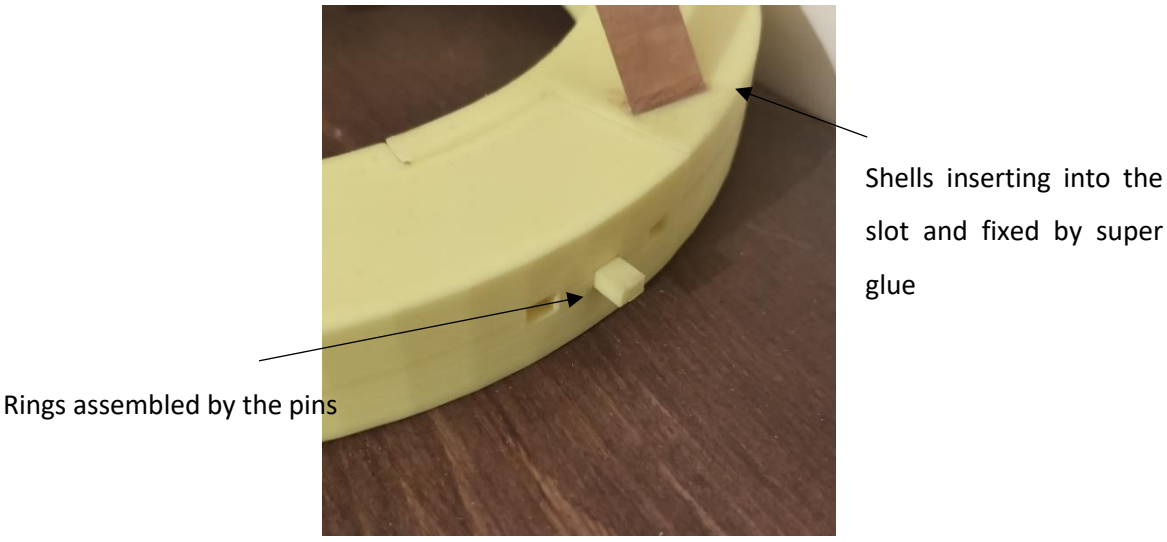
The prototype consists of two rings fixed on the femur and tibia, respectively, and two compliant shells cross-linked on the rings. The compliant shells bought online are made of beryllium bronze, chosen for its flexural characteristics. The segments of rings were manufactured by an Ultimaker S5 3D printer with simple setup, high uptime, and reliable dual extrusion. The printing material is Standard PLA, which is a 100 percent annually renewable biodegradable material that is easier on the environment. The printer technical specifications are summarized in Table 6. Considering the time and material saving, only 40 percent of the rings are printed by the 3D printer, which means the other 60 percent of solid part are empty. Finally, assemble the rings by the adjustable slots and shells with super glue shown in Fig. 32.

Table 6 The printer technical specifications.

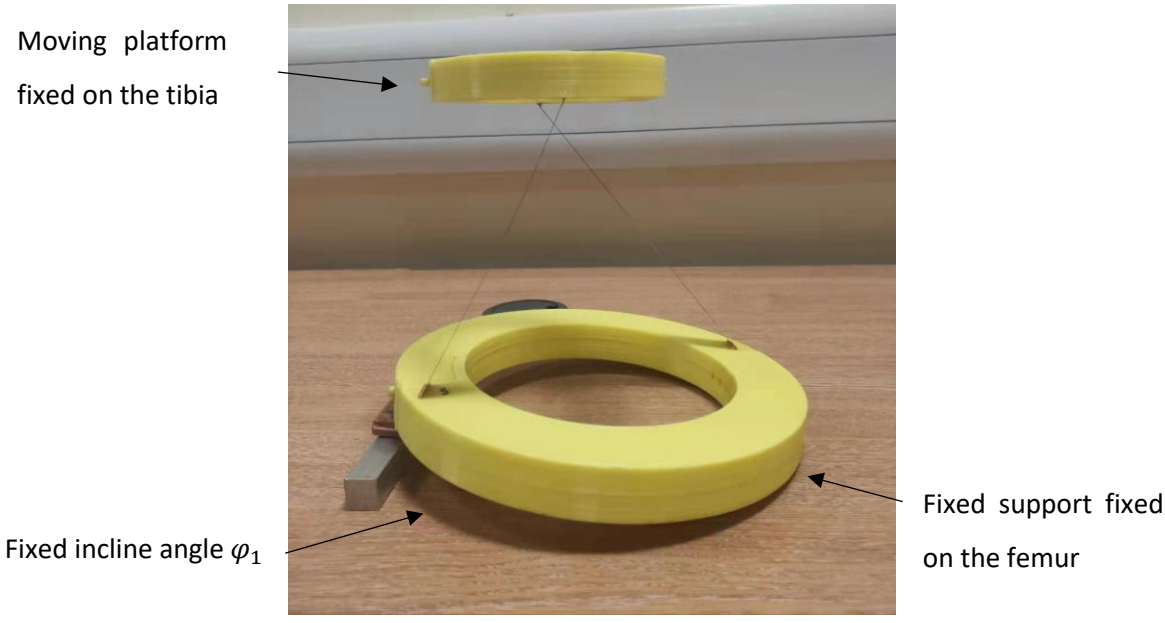
Print technology	Fused filament fabrication (FFF)
Compatible filament diameter	2.85 mm
Maximum power output	500 W
Build speed	<24 mm^3/s
Operation ambient temperature	15-32 ℃ (59 − 90°F)



a



b



c

Figure 32 Prototype: **a**, **b** the local details of the device, and **c** the assembled mechanism.

5.2.2. Demonstration

The prototype, test device used for wearing on the knee joint is not of the correct size, we demonstrate the prototype on the elbow joint just for the test. As Fig. 33 shows, there is an inclining angle of the femur part simulation which will be considered during experiment such as adding a slope on the one side shown below. The diagram illustrates the states of extension and flexion of the joint, and the position of the elbow corresponds to the rotational centre shown in Fig. 33. While the size of the rings must be fitted human knees in the future applications.

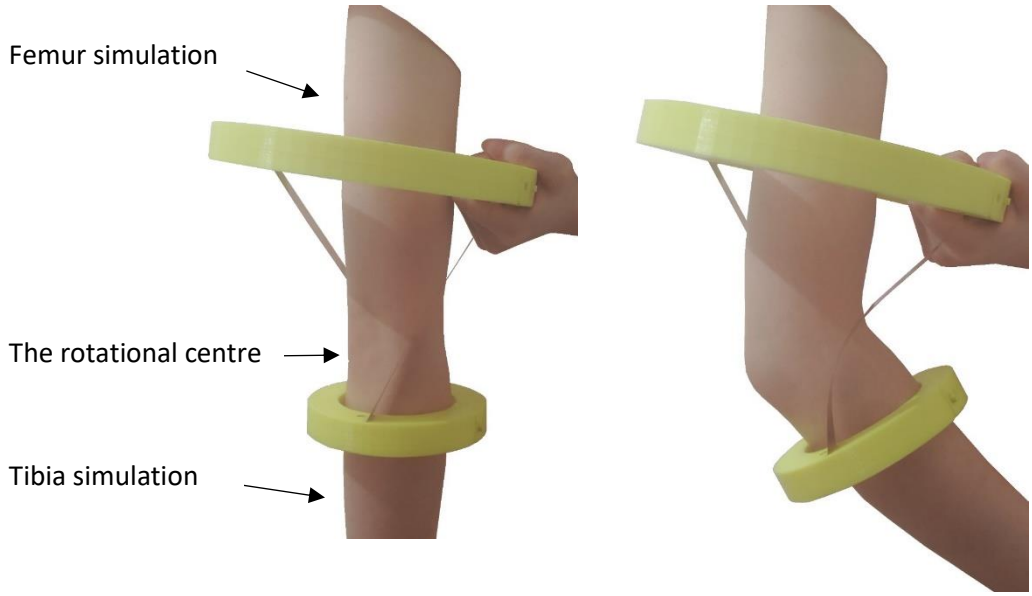


Figure 33 The demonstration.

5.2.3. Testing

1. The goal of the experiment:

Use some weights exerting on the moving platform and obtain the rotational angle of the platform. Then, compare the experimental results with the theoretical values and FEA results, verifying the rotational stiffness.

2. Experimental materials

The experimental set-up includes the wearable device, some weights (10 grams of each), and a protractor tool, which is elaborated in Fig. 34. Due to the use of rough materials and experimental method, the results are subject to error.



Figure 34 Experimental materials.

3. Experimental process

Add the 10 grams (g) weights successively on the moving platform, and measure the rotational angles of it by protractor tool. Fig. 35 shows the effect of adding 10g, 20g, and 30g weights on the platform, respectively, and 30g is the limit of the shells.

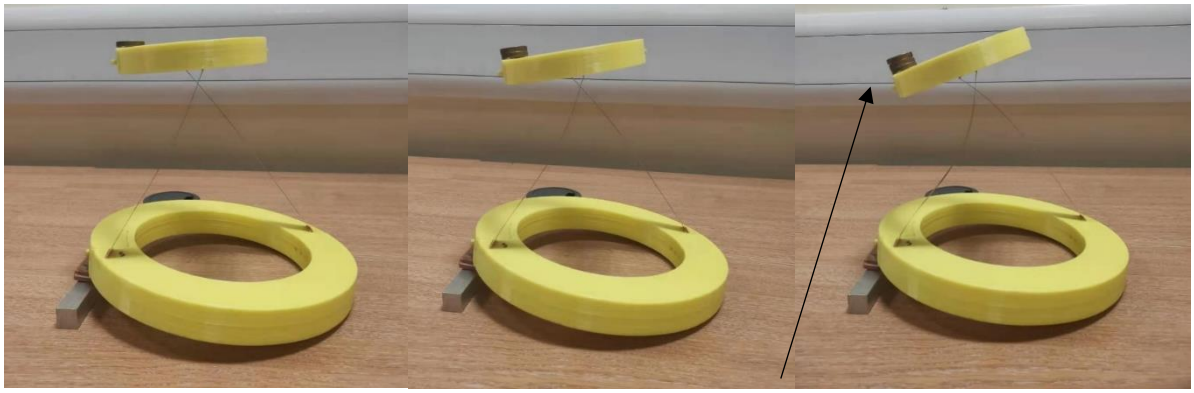


Figure 35 Experimental process: **a**, **b**, **c** Adding 10g, 20g, and 30g weights on the platform, respectively.

4. Experimental results

Table 7 The experimental results.

Weights (g)	Rotational angle (degrees)
10	5
20	10
30	20

The experimental results are shown in Table 7. The actuation force is achieved by applying a series of weights on the moving platform. It seems pretty clear that the slope between group1 to 2 and group 2 to 3 is different, which illustrates the group 3 (30-gram weights) is non-linear which demonstrates that buckling happens when adding 30 g weights.

One can transform the force-rotation relationship to the moment-rotation relationship through $M = F \cdot d$, where M is the moment; F is the force exerted by weights; d is the distance from force to rotational centre, the moment-rotation relationship shown in Fig. 36. The moment on the moving platform increases as the rotation grows, and the maximum moment is about 0.015 ($N \cdot m$) when adding 30 g weights. However, there are no more experimental groups due to the limitation of the weights. Thus, the accuracy of experiment may be affected.

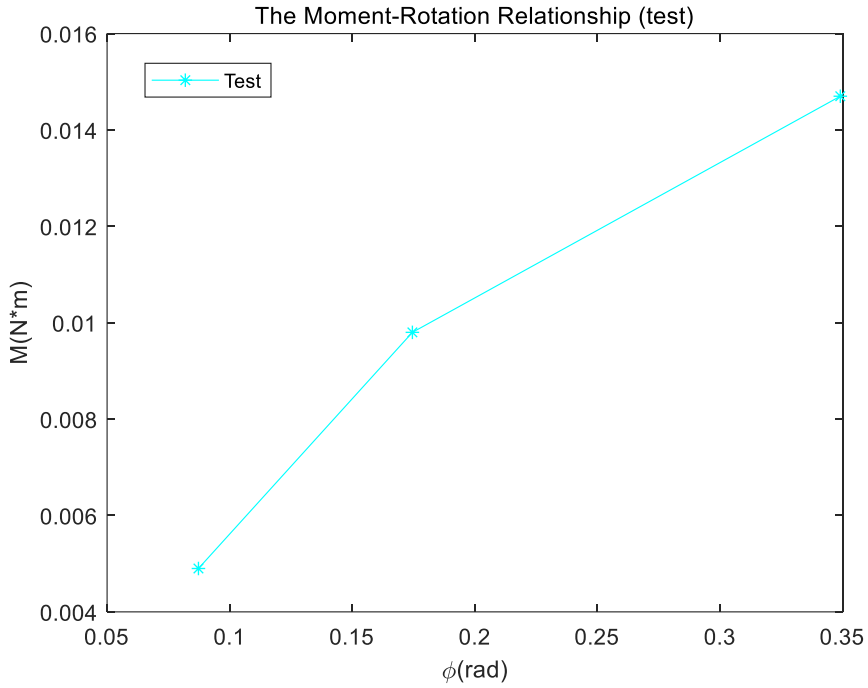
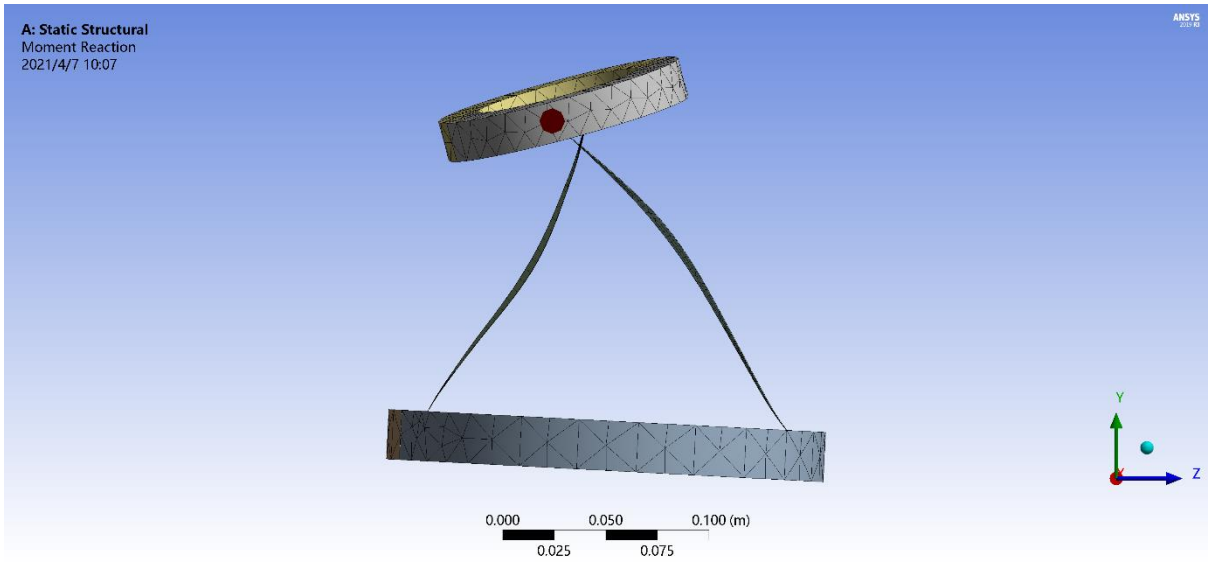


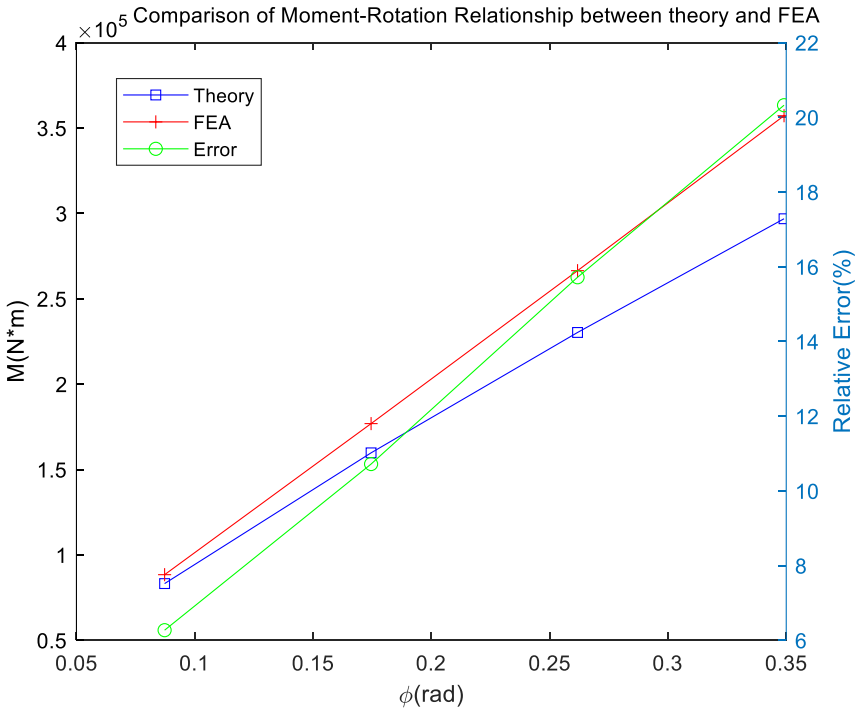
Figure 36 Experimental results.

To prove the precision of the test as well as the performance of the four-bar linkage, the model was calculated in the theoretical calculation and simulated in the FEA software. Transform force into the moment of the test and substitute them and the geometric parameters into the theoretical equation deduced in Eq. (3-22), getting the theoretical results. Simulate in Comsol 5.0, assume that the crossed shells are elastic and the two platforms are

rigid. The material of shells is beryllium bronze the same as the test, material parameters listed before. The meshing and analysis setting performs the same as 4.2.2. A series of rotations range from 0 to 20 degrees with a 5 degrees step are prescribed on the moving platform. The results for the FEA solution are illustrated in Fig. 37a, and the comparison between theoretical and FEA results are demonstrated in Fig. 37b.



a



b

Figure 37 Comparison between FEA and experimental results: **a** the FEA simulation, and **b** the comparison between theoretical, FEA results and the bio-joint.

The theoretical and FEA results are graphically presented in Fig. 37b. The results indicate a good agreement among the two methods, as the rotation increases, the moment also increases. The largest moments reach $3 \times 10^5\ (N \cdot m)$ and $3.5 \times 10^5\ \ (N \cdot m)$ for theoretic and FEA results, respectively, and the maximum deviation between them is about 20 percent difference. In all the above figures, the theoretical data is in good agreement with the data obtained by FEA, while the experimental data is quite different from them. The reasons and improvements will be discussed in the next section.

5.3. Discussions

Through the above comprehensive analysis, we can conclude that the results of FEA, theoretical value are relatively consistent, which proves that the flexural-hinge replaced four-bar linkage are well fitted to apply on knee rehabilitation. However, the experimental results are dramatically different from them. Besides the manufacturing accuracy and assembly error, the limitation of external loads adding is a vital factor.

Considering the self-weight of the moving platform which leads to shell rotating and twisting before adding loads, we propose an inversion-four-bar linkage whose upper end of the shells link to the lower platform and the lower end of shells link to the upper platform, conversely, shown as Fig. 38. In this mechanism, the shells will not suffer the loads from the upper platform and are supported by the fixed platform, which gives rise to reducing the error of the results and expands the experimental datum.

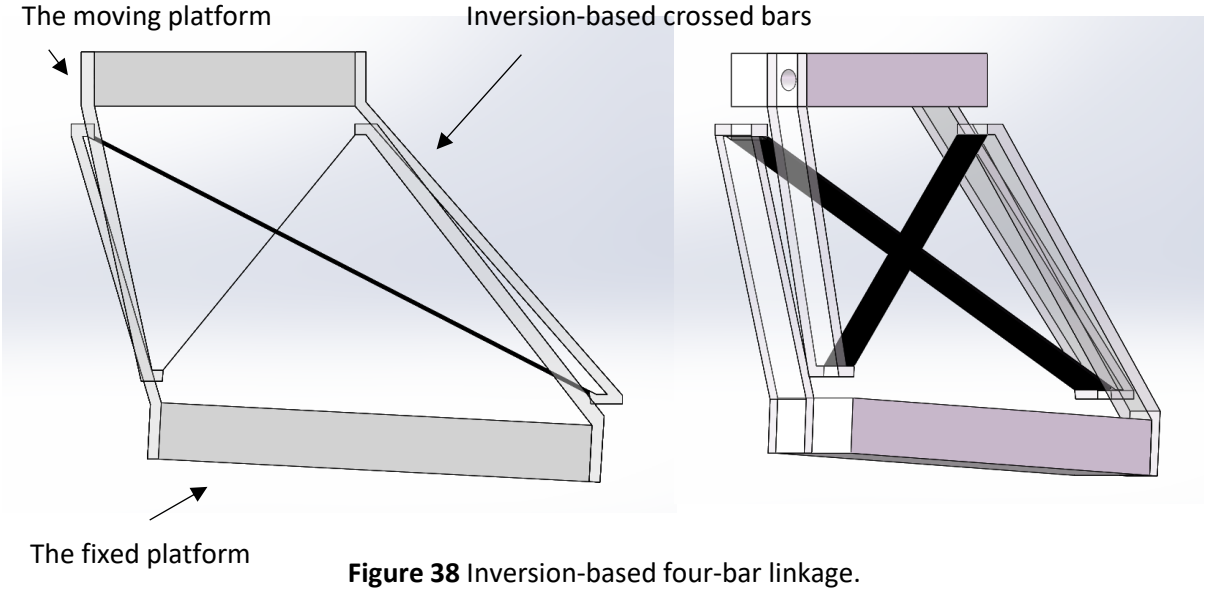


Figure 38 Inversion-based four-bar linkage.

Another improvement is to leave the extra allowance of the slot, in case the error of the depths or angles of insertions influence the experimental results. The perimeters of the rings fixed on the femur and tibia should be larger than the leg circumferences as well, due to the machining imperfections.

6. Future work and conclusions

6.1. Future work

The current device has a number of a backlog of defects such as incompatibility for legs, buckling limitation of the shells and machining imperfections. Therefore, we should improve the model as follow:

1. Determine the circumferences of the femur and tibia, and leave the suitable allowance of perimeters of rings.

2. Investigate the model proposed in Fig. 38. Analyze the kinematics and kinetostatic of the inversion-based four-bar linkage, comparing with non-inversion one and optimizing the parameters to mimic a bio-joint. Finally, fabricate the model and do the test to verify the accuracy of the model.

In addition, it is proposed to utilize flexural four-bar linkage on other human joints' rehabilitation which has similar motion characteristics. Taking advantage of lightweight materials and portability, this model may be extensively applied to human joints' rehabilitation.

6.2. Conclusions

Through the work carried out on this project, a lightweight, compliant wearable mechanism for knee rehabilitation has been developed which improves the drawback of the existed devices. This device follows the trajectory of the knee motion and used the compliant mechanism creatively, which offers cost savings, greater efficiency and improves accuracy and reliability. The major characteristics of the device are described via a combinatory method including theoretical and FEA model. Based on the PRBM, a flexural four-bar linkage is presented to serve as the kinematic model of the compliant wearable mechanism. A parametric model of the wearable mechanism has been developed to facilitate the design and optimization, which has been compared with FEA and experimental results. Although there is a derivation between analytical and experimental results, the improvement discussed above may address these issues.

The wearable compliant mechanism has the potential to help people with knee problems as well as infusing the healthcare system with the prospect of developing new opportunities. Thanks to the support by the academic and governmental agency.

7. References

[1] Chen, Bing, et al. "Knee exoskeletons for gait rehabilitation and human performance augmentation: A state-of-the-art." Mechanism and Machine Theory 134 (2019): 499-511.

[2] Zhou, Libo, et al. "Design of a lower limb rehabilitation robot based on 3-RPR parallel mechanism." 2017 29th Chinese Control And Decision Conference (CCDC). IEEE, 2017.

[3] Bai, Kun, et al. "Design of a compliant knee-motion actuator for lower extremity exoskeletons." 2016 IEEE International Conference on Advanced Intelligent Mechatronics (AIM). IEEE, 2016.

[4] Yuan, Bo, et al. "Designing of a passive knee-assisting exoskeleton for weight-bearing." International Conference on Intelligent Robotics and Applications. Springer, Cham, 2017.

[5] https://sms.hest.ethz.ch/research/past-research-projects/lower-limb-exoskeletons-and-exosuits.html

[6] Zhang, Li, et al. "Assistive devices of human knee joint: A review." Robotics and Autonomous Systems 125 (2020): 103394.

[7] Chaichaowarat, Ronnapee, et al. "Passive knee exoskeleton using torsion spring for cycling assistance." 2017 IEEE/RSJ International Conference on Intelligent Robots and Systems (IROS). IEEE, 2017.

[8] Ranaweera, R. K. P. S., et al. "Development of a passively powered knee exoskeleton for squat lifting." Journal of Robotics, Networking and Artificial Life 5.1 (2018): 45-51.

[9] Kim, Jung-Hoon, et al. "Design of a knee exoskeleton using foot pressure and knee torque sensors." International Journal of Advanced Robotic Systems 12.8 (2015): 112.

[10] Kuan, Jiun-Yih, Kenneth A. Pasch, and Hugh M. Herr. "Design of a knee joint mechanism that adapts to individual physiology." 2014 36th Annual International Conference of the IEEE Engineering in Medicine and Biology Society. IEEE, 2014.

[11] Celebi, Besir, Mustafa Yalcin, and Volkan Patoglu. "AssistOn-Knee: A self-aligning knee exoskeleton." 2013 IEEE/RSJ International Conference on Intelligent Robots and Systems. IEEE, 2013.

[12] Sridar, Saivimal, et al. "A soft-inflatable exosuit for knee rehabilitation: Assisting swing phase during walking." Frontiers in Robotics and AI 5 (2018): 44.

[13] Lee, Younbaek, et al. "Biomechanical design of a novel flexible exoskeleton for lower extremities." IEEE/ASME Transactions on Mechatronics 22.5 (2017): 2058-2069.

[14] Choi, Byungjune, et al. "A self-aligning knee joint for walking assistance devices." 2016 38th Annual International Conference of the IEEE Engineering in Medicine and Biology Society (EMBC). IEEE, 2016.

[15] Lee, Kok-Meng, and Donghai Wang. "Design analysis of a passive weight-support lower-extremity-exoskeleton with compliant knee-joint." 2015 IEEE International Conference on Robotics and Automation (ICRA). IEEE, 2015.

[16] Olinski, M., et al. "Design and characterization of a novel knee articulation mechanism." International Journal of Applied Mechanics and Engineering 21.3 (2016).

[17] Bertomeu, José María Baydal, et al. "Development of a hinge compatible with the kinematics of the knee joint." Prosthetics and orthotics international 31.4 (2007): 371-383.

[18] R. Lin, W. Guo, F. Gao. “On Parasitic Motion of Parallel Mechanisms”, in ASME International Design Engineering Technical Conferences and Computers and Information in Engineering Conference, Charlotte, NC, USA, 2016.

[19] Lee, Kok-Meng, and Jiajie Guo. "Kinematic and dynamic analysis of an anatomically based knee joint." Journal of biomechanics 43.7 (2010): 1231-1236.
[20] Menschik, A. "Mechanik des Kniegelenkes. i." (1974).
[21] Hirschmann, Michael T., and Werner Müller. "Complex function of the knee joint: the current understanding of the knee." Knee Surgery, Sports Traumatology, Arthroscopy 23.10 (2015): 2780-2788.
[22] Müller W. The knee: form, function, and ligament reconstruction[M]. Springer Science & Business Media, 1983.
[23] Iwaki, H., V. Pinskerova, and M. A. R. Freeman. "Tibiofemoral movement 1: the shapes and relative movements of the femur and tibia in the unloaded cadaver knee." The Journal of bone and joint surgery. British volume 82.8 (2000): 1189-1195.
[24] Nomiyama, T., et al. "Model analysis of lower limb at deep knee flexion." Proceedings of the International Conference on Electrical Engineering and Informatics. 2007.
[25] Hongzhe, Z. H. A. O., and Bi Shusheng. "Accuracy characteristics of the generalized cross-spring pivot." Mechanism and Machine Theory 45.10 (2010): 1434-1448.
[26] Hubbard, Neal B., et al. "A novel fully compliant planar linear-motion mechanism." International Design Engineering Technical Conferences and Computers and Information in Engineering Conference. Vol. 46954. 2004.
[27] Simon, H., S. Peter, and D. Serge. "Flexure Pivot for Aerospace Mechanisms, 10th European Space Mechanisms and Tribology Symoposium." San Sebastian, Spain (2003).
[28] Zhao, Hongzhe, Shusheng Bi, and Jingjun Yu. "A novel compliant linear-motion mechanism based on parasitic motion compensation." Mechanism and Machine Theory 50 (2012): 15-28.
[29] Zelenika, Saša, and Francesco De Bona. "Analytical and experimental characterisation of high-precision flexural pivots subjected to lateral loads." *Precision Engineering* 26.4 (2002): 381-388.
[30] Wittrick, W. H. "The properties of crossed flexure pivots, and the influence of the point at which the strips cross." *Aeronautical Quarterly* 2.4 (1951): 272-292.
[31] Ryu, Jae W., and Dae-Gab Gweon. "Error analysis of a flexure hinge mechanism induced by machining imperfection." *Precision Engineering* 21.2-3 (1997): 83-89.
[32] Zhao, Hongzhe, and Shusheng Bi. "Stiffness and stress characteristics of the generalized cross-spring pivot." *Mechanism and Machine Theory* 45.3 (2010): 378-391.
[33] Hongzhe, Z. H. A. O., and Bi Shusheng. "Accuracy characteristics of the generalized cross-spring pivot." Mechanism and Machine Theory 45.10 (2010): 1434-1448.
[34] Karami, M., Gérard Maurice, and J. M. Andre. "A model of exo-prosthesis of the knee optimized with respect to the physiological motion of condyles." ITBM-RBM 25.3 (2004): 176-184.
[35] Midha, Ashok, Zhen-Lu Zhao, and I. Her. "Mobility conditions for planar linkages using triangle inequality and graphical interpretation." (1985): 394-399.
[36] Angeles, J., and A. Bernier. "A general method of four-bar linkage mobility analysis." (1987): 197-203.
[37] Bai, Shaoping. "Geometric analysis of coupler-link mobility and circuits for planar four-bar linkages." Mechanism and Machine Theory 118 (2017): 53-64.
[38] Howell, Larry L. "Compliant mechanisms." 21st century kinematics. Springer, London, 2013. 189-216.
[39] Junior, LA Gonçalves, et al. "Theoretical and experimental investigation of performance characteristics and design aspects of cross-spring pivots." International Journal of Solids

and Structures 185 (2020): 240-256.

8. Appendices

8.1. Matlab code for optimizing cross-spring pivot

```
L=0.06;
T=0.0005;
W=0.006;
format  shortE
E=0.73e+11;
I=1/12*T*W^3;
d=12*(L/T)^2;
p=0;
alpha=45/180*pi;

a=zeros(1,99);
b=zeros(1,99);
c=zeros(1,99);
count=0;

for lambda=0:0.1:1
    for theta=0/180*pi:10/180*pi:80/180*pi
    count=count+1;

    y = -0.0023*theta.^5 + 0.017*theta.^4 -
0.045*theta.^3 + 0.045*theta.^2 + 0.00099*theta + 0.0029;

    dx=(-1/cos(alpha).*(1/150.*(9.*lambda.^2-
9.*lambda+1).*(12.*lambda-
1).*theta.^3+6.*cot(alpha).^2.*(2.*lambda-
1).*(theta./d+1/6300.*(9.*lambda.^2-
9.*lambda+11).*theta.^3))-(12.*lambda-
1)./(20.*sin(alpha).^2).*(theta./d+1/6300.*(9.*lambda.^2-
9.*lambda+11).*theta.^3).*p).*(lambda>=0&lambda<=0.5)+(1/
cos(alpha).*(1/150.*(1-12.*lambda).*(9.*lambda.^2-
9.*lambda+1).*theta.^3+6.*cot(alpha).^2.*(1-
2.*lambda).*(theta./d+1/6300.*(9.*lambda.^2-
9.*lambda+11).*theta.^3))+((11-
12.*lambda)./20.*(1./sin(alpha).^2+theta.^2./cos(alpha).^
2)-1/2.*(1/sin(alpha).^2-
1/cos(alpha).^2)).*(theta./d+1/6300.*(9.*lambda.^2-
9.*lambda+11).*theta.^3).*p).*(lambda>0.5&lambda<=1)

    dy=(1/(2.*cos(alpha)).*(-2/15.*(9.*lambda.^2-
9.*lambda+1).*theta.^2+1/1500.*(2592.*lambda.^4-
3024.*lambda.^3+1338.*lambda.^2-
241.*lambda+2).*theta.^4)+1/(2.*cos(alpha).^2).*(1/d+1/63
```

```
00.*(9.*lambda.^2-
9.*lambda+11).*theta.^2).*p).*(lambda>=0&lambda<=0.5)+(-
1/(15.*cos(alpha)).*(9.*lambda.^2-
9.*lambda+1).*theta.^2+1./cos(alpha).*(1/3000.*(2592.*lam
bda.^4-5184.*lambda.^3+3678.*lambda.^2-
1511.*lambda+447)+cot(alpha).^2.*(1-
2.*lambda)./1050.*(9.*lambda.^2-
9.*lambda+11)).*theta.^4+((11-
12.*lambda)./20.*(1./cos(alpha).^2-
1./sin(alpha).^2).*theta.^2+1/2.*(1./cos(alpha).^2+theta.
^2./sin(alpha).^2)).*(1./d+1./6300.*(9.*lambda.^2-
9.*lambda+11).*theta.^2).*p).*(lambda>0.5&lambda<=1)

    a(:,count)=dx;
    b(:,count)=dy;
    c(:,count)=y;

    end
end

d=sqrt(a.^2+b.^2);
diff=c-d;

g=zeros(1,9);
count=0;
m=1;
n=m+9;
while n<=99
count=count+1;
difsum=sum(diff(m:n));
g(:,count)=difsum;
m=n+1;
n=m+9;

end
g
```

8.2. Matlab code for optimizing four-bar linkage

```
r1=0.164;
r2=0.158;
r3=0.022;
r4=0.2;

a=zeros(1,45);
b=zeros(1,45);
count=0;
for phi1=0/180*pi:5/180*pi:20/180*pi
    for phi3=0/180*pi:10/180*pi:80/180*pi
    count=count+1;
    Xa=0;
    Ya=0;
    Xd=r1*cos(phi1);
    Yd=-r1*sin(phi1);

    C1=Xd+r3.*cos(phi3);
    C2=Yd+r3.*sin(phi3);

    A=2.*C2.*r4;
    B=2.*C1.*r4;
    C=r2.^2-r4.^2-C1.^2-C2.^2;

    phi4=(real( 2.*atan((A + (A.^2 + B.^2 -
C.^2).^(1/2))./(B +
C))).*(phi3>=0/180*pi&phi3<=100/180*pi)+(2*pi+real(
2.*atan((A + (A.^2 + B.^2 - C.^2).^(1/2))./(B +
C)))).*(phi3>100/180*pi&phi3<=120/180*pi));

phi2=(atan((r4.*sin(phi4)+C2)./(r4.*cos(phi4)+C1)).*(phi3
>=0/180*pi&phi3<=60/180*pi)+(pi+atan((r4.*sin(phi4)+C2)./
(r4.*cos(phi4)+C1))).*(phi3>60/180*pi&phi3<=100/180*pi)+(
pi+atan((r4.*sin(phi4)+C2)./(r4.*cos(phi4)+C1))).*(phi3>1
00/180*pi&phi3<=120/180*pi));

    Xc=r2.*cos(phi2)-r3.*cos(phi3);
    Yc=r2.*sin(phi2)-r3.*sin(phi3);
    Xb=r2.*cos(phi2);
    Yb=r2.*sin(phi2);

    a1 =(Ya - Yb)./(Xa - Xb);
    b1 =(Xa.*Yb - Xb.*Ya)./(Xa - Xb);
    a2 =(Yc - Yd)./(Xc - Xd);
    b2 =(Xc.*Yd - Xd.*Yc)./(Xc - Xd);
```

```
    X =-(b1 - b2)./(a1 - a2);
    Y =(a1.*b2 - a2.*b1)./(a1 - a2);
    a(:,count)=X;
    b(:,count)=Y;
    end
end
a
b
```